JOURNAL OF COMPUTATIONAL PHYSICS 107, 124–145 (1993)

A Simulation of Low-Frequency Electromagnetic Phenomena in Kinetic Plasmas of Three Dimensions

MOTOHIKO TANAKA

National Institute for Fusion Science, Nagoya 464-01, Japan

Received November 19, 1991; revised October 21, 1992

An advanced kinetic simulation method has been developed and implemented in the HIDENEK code to study large space-scale, low-frequency electromagnetic phenomena occurring in inhomogeneous plasmas. The present method is specially designed for high magnetic field ($\omega_{ce} \gtrsim \omega_{pe}$), inhomogeneous plasma simulations. The guiding-center approximation with magnetic drifts is adopted to the perpendicular motion of the electrons, whereas the inertia effect is retained in their parallel motion. Also, a slightly backward time-decentered scheme is introduced to the equations of motion and the Maxwell equations. These equations are combined to yield the full-implicit, coupled field-particle equations which allow us to determine the future electromagnetic field in a large time step compared to the electron time scales with the diamagnetic drift and magnetization currents being included. As a demonstration of the present simulation method, three physics applications are shown for the electromagnetic beam–plasma instability, the temperature anisotropy-driven Alfven-ion-cyclotron instability, and the external kink instability of the peaked-density current beam. A remarkable pitch-angle scattering of the ions is observed in the first two applications in association with the plasma instabilities. In the third application to an inhomogeneous, finite-beta plasma of the three dimensions, a helical deformation is shown to take place to the initially straight beam and magnetic axis in an ideal magnetohydrodynamic time scale.

1. INTRODUCTION

A fully nonlinear evolution of the low-frequency, kinetic instabilities and associated transport of energy and particles in plasmas have remained an important but unresolved issue of plasma physics for more than past two decades. In the meantime, as an origin of these instabilities and transport a certain realm of the high-temperature plasmas has attracted our attention in which microscopic, kinetic processes strongly affect macroscopic plasma characteristics and processes with magnetohydrodynamic (MHD) time-and-space scales.

Concerning the above statement, many significant phenomena of space and fusion plasmas are known to take place in this kinetic and macroscopic regime. For example, ion kinetic effects on the $m=1$ kink mode [1] and behaviors of fusion-produced energetic alpha particles [2] in ignited tokamaks are just a few of important low-frequency, kinetic problems of the magnetically confined fusion plasmas. In space and astrophysics, we can find more varieties of such plasma phenomena. We list, to name only a few, magnetic reconnection—an active agent of magnetic energy release whose dissipation layer has a thickness comparable to gyroradius or inertia length of ions [3], and the kinetic Alfven wave which induces substantial wave–particle interactions with its longitudinal (non-MHD) electric field [4].

Since the aforementioned plasma phenomena are frequently accompanied by strong nonlinear processes, a numerical simulation has been considered to be the only one reliable approach for theoretical studies. However, until recently it was quite difficult to study these nonlinear plasma processes using either the conventional time-explicit/hybrid particle codes or the MHD fluid code. This was precisely attributed to both a kinetic nature of such plasmas and a disparity of their time-and-space scales with currently uninteresting high-frequency, short-wavelength plasma eigenmodes or light waves. By contrast, during the entire 1980s several types of new and advanced simulation methods were devised in order to overcome the difficulties. These research results are well-documented in Ref. [5–8]. As will be briefly reviewed in this section, the new simulation methods were successfully applied to various nonlinear phenomena in high-temperature plasmas.

To summarize, what has been required to the new type of the kinetic, large MHD-scales simulation methods is an ability to treat (1) various kinetic (particle) effects such as the Landau, cyclotron, and bounce resonances with low-frequency waves and those due to finite Larmor radius and complicated particle trajectories, (2) a space-charge electric field and a finite-speed plasma relaxation arising from non-zero electron inertia, and (3) nonlinear plasma processes under the non-microscopic time-and-space scales, i.e.,

0021-9991/93 $5.00

(duration time) $\gg \omega_{pe}^{-1}$, ω_{ce}^{-1} and (spatial scale) $\gg \lambda_e$, ρ_e. Here, ω_{pe}, ω_{ce} are the plasma and cyclotron frequencies, respectively, and λ_e, ρ_e are the Debye and gyroradius of the electrons. Moreover, it should be emphasized that magnetically confined plasmas are often strongly magnetized ($\omega_{ce} \geqslant \omega_{pe}$) and quite inhomogeneous; the strength and orientation of the magnetic field changes in space and time. The electron diamagnetic drift and magnetization currents are important in the finite-beta (temperature) plasmas. In fact, these (equivalent) drift velocities are given by $v_D \sim (cT_e/eB)/\lambda_0 = \frac{1}{2} c\beta_e(\omega_{ce}/\omega_{pe})(c/\lambda_0\omega_{pe})$, where $\beta_e = 8\pi n T_e/B^2$ is the electron beta value and λ_0 is the gradient scale length of density or the ambient magnetic field.

The new particle simulation methods developed in early 1980s have realized kinetic simulations of the low-frequency, electromagnetic phenomena while eliminating the high-frequency electron plasma oscillations. However, a difficulty with those methods was a small time step $\omega_{ce}\,\Delta t \leqslant O(0.1)$ in order to reproduce the diamagnetic and magnetization effects of the electrons in high magnetic field, high-beta plasmas. The uniqueness of the present implicit particle simulation method, on the contrary, is its ability to treat these diamagnetic drift and magnetization effects under a much larger time step $\omega_{ce}\,\Delta t \gg 1$. This permits us more efficient and accurate simulations of strongly magnetized, high-beta plasmas with much less time steps. (It is also possible for the present method to choose the full-kinetic electrons where the ambient magnetic field is weak or absent (cf. Section 2.1)). In the following paragraphs, several large time-and-space scale, kinetic simulation methods are briefly reviewed.

The first successful implicit simulation method might be *the moment implicit method* which derives the implicit moment equations to obtain the future electromagnetic field [9–11]. The moment equations involve a divergence of the pressure tensor which, by relying on the fluid concept, is related to the particle velocity moments to achieve a closure of the moment equations. The velocity moments are calculated once in each time step by summations over the particles. This class of the particle code known as the "VENUS" code was developed at Los Alamos National Laboratory in early 1980s and was applied to laser irradiation and various beam–plasma processes [12]. However, the assumptions used in relating the pressure tensor with the particle moments restricted the time step to a moderate value $\omega_{pe}\,\Delta t \leqslant 10$ in warm kinetic plasma simulations. An improved method has recently outgrown from the moment implicit method to treat the warm plasmas with a large time step and several demonstrations have been made for one-dimensional plasmas (CELEST) [13].

The closely-coupled implicit method, which is a subject of this paper, was devised in early 1984 as an electromagnetic simulation method for multi-dimensional plasmas by following the intuition that the futureward time-shifted electromagnetic field might act to preferentially suppress high frequency oscillations in the plasma [7]. Now this method satisfies the aforementioned three requirements and an additional one for the advanced large-scale kinetic simulation methods [14]. The technically most characteristic feature of this implicit method, which has been implemented in the HIDENEK (hyper-implicit, decentered, and kinetic) code, is a direct determination of the future electromagnetic field using completely implicit, coupled kinetic equations. Here, a predictor–corrector particle push is not used to obtain unknown current and charge densities which act as driving forces in the field equations. Hence, these coupled kinetic equations are named "closely-coupled field-particle (CCFP) equations."

Another type of the implicit electromagnetic particle simulation method which is called *the direct implicit method* was developed at Livermore National Laboratory and the University of Texas [15, 16]. This method constructs a high-accuracy low-pass time filter by combining the electric acceleration of a few time levels in the equations of motion to control numerical damping of high-frequency waves in the plasma. The future current density is explicitly predicted by pushing particles and is implicitly corrected later in the field equations. A recent progress in the filtering technique is found in Ref. [17]. Basically, the direct implicit method has the second-order (or more) accuracy in time, however, it suffered from substantial and monotonic loss of the particle kinetic energy during the course of the two-dimensional simulation [16].

The gyrokinetic particle simulation method [8] which was motivated at the Princeton Plasma Physics Laboratory is conceptually different from the implicit particle methods in that it derives reduced field equations by gyro-averaging the ion response under assumptions of smallness on the wavelength and frequency $k_{\|}/k_{\perp} \ll 1$, $\omega/\omega_{ci} \ll 1$ and those on the amplitude of the electromagnetic field. Many insignificant terms are removed from the original kinetic equations. Efficiency and accuracy of the simulation are therefore quite reasonable when the ordering assumptions are satisfied. However, when the assumptions become marginally satisfied, which occurs with large electrostatic disturbances $e\delta\varphi/T_e \sim O(1)$ at the plasma edge, for example, or magnetic perturbations $\delta B/B_0 \sim O(1)$ at the magnetic reconnection, many correction terms are required to make the simulation physically meaningful.

As possibly a comparable kinetic simulation method with the implicit particle methods, *the hybrid particle code* with particle ions and massless electrons is sometimes used for the study of low-frequency electromagnetic phenomena [18]. The hybrid code is quite efficient since the electron kinetic effects are excluded and is therefore considered to be valid when the electron inertia effects are completely ignorable. This is the case with a simulation of the perpendicular magnetosonic shock where the plasma is

strongly magnetized with the magnetic field lying perpendicularly to the simulation plane [19]. However, the hybrid code becomes increasingly unjustifiable as the magnetic field becomes more oblique or parallel to the simulation plane so that the electrons are allowed to move along the ambient magnetic field in an inhomogeneous medium.

In the following two paragraphs, the essence of the closely-coupled implicit method is qualitatively described in some depth. There was a preliminary ("semi-implicit") version which was first developed and applied to variety of large space-scale simulations such as an excitation of the kinetic Alfven wave and associated plasma heating [20], and current-beam injection and kink instability [21]. However, the time step was limited to $\omega_{pe}\,\Delta t \leqslant 1$. Qualitatively a much improved version that can deal with "homogeneous" kinetic plasmas in large time-and-space scales was then developed [7]. The characteristics of the algorithm were extensively studied and its validity was proved both analytically and numerically in the literature. Recently the latter version of the code has greatly been upgraded so that it can efficiently deal with high magnetic field, high-beta kinetic plasmas in large MHD-scales [14]. Specifically, the guiding-center approximation with the magnetic effects has been introduced to the electron motion. The parallel motion along the magnetic field line is traced as particles in a drift-kinetic fashion with $-\mu\nabla_{\|}B$ force included. This enables us the treatment of the diamagnetic and magnetization currents while eliminating both the high-frequency electron cyclotron and plasma oscillations. These time scales are of the same orders of magnitude in the magnetically confined plasmas.

The key of the closely-coupled implicit method consists in its complete time-implicitness. By combining the Maxwell equations with the equations of motion of particles, the closely-coupled field-particle equations are derived which directly determine the future electromagnetic field without an auxiliary prediction of the current and charge densities. These equations are solved actually in the real (configuration) space because the implicitly-expressed current and charge densities, which are the major driving terms of the equations, vary considerably in space for inhomogeneous plasmas. This makes the solution in the Fourier-space difficult and inefficient. The characteristic features of the closely-coupled implicit method are summarized in Table I. The fundamentally important feature here is that the low-frequency electromagnetic waves and structures with $\omega_0\,\Delta t \ll 1$ are properly reproduced, where ω_0 is their characteristic frequency and Δt is the time step of the simulation. Since the ions and electrons are handled as the particle species, various particle orbit effects are well simulated by this method. Moreover, the method works numerically well, both in the linear and nonlinear stages of the plasma processes by virtue of the slightly backward time-decentered scheme. These advanced features make the closely-coupled implicit method quite suitable for studies of kinetic and nonlinear plasma phenomena occurring in large time-and-space scales.

The outline of this paper is the following. In Section 2, the implicit algorithm of the closely-coupled implicit method is described in detail, which has been implemented in the HIDENEK code for the study of low-frequency electromagnetic phenomena in high magnetic field, inhomogeneous plasmas of multi-dimensions. A key approximation and numerical methods are introduced in Section 3 which permit us solution of the closely-coupled field-particle equa-

TABLE I

Characteristics of the HIDENEK Simulation Code

- Large time-and-space scales: $\omega_{pe}\,\Delta t \gg 1$, $\omega_{ce}\,\Delta t \gg 1$, and $\Delta x \geqslant c/\omega_{pe}$.
- Electromagnetic.
- Multi-dimensions in any geometry (Cartesian, cylinder, torus).
- Inhomogeneous plasma density and magnetic field.
- Kinetic:

  Ions: Full 3D particle dynamics.
  Electrons: Parallel direction → 1D motion with $(-\mu\nabla_{\|}B)$ force.
  Perpendicular direction → Guiding-center drift motion.
  ($\mathbf{E}\times\mathbf{B}$, ∇B, curvature drifts)

  → Resonance effects (Landau, cyclotron, bounce resonances)
  Orbit effects: Finite Larmor radius effects
  Diamagnetic and magnetization effects
  Complicated particle trajectories
  Finite speed relaxation due to electron inertia
  } included.

tions under the limited computing resources. Numerical stability and energy conservation are also discussed. Three physics applications to the low-frequency, large-scale kinetic plasmas are described in Sections 4–6. Especially in Section 6, a three-dimensional simulation of the kink instability is shown, where a finite-amplitude helical perturbation develops to the initially pressure-balanced, inhomogeneous plasma with a concentrated axial current. Section 7 makes a summary of the paper and gives several important remarks and the procedure of the parameter design concerning the closely-coupled implicit method.

2. IMPLICIT ALGORITHM FOR THE LOW-FREQUENCY KINETIC PLASMA SIMULATION

This section first presents the fundamental equations governing the electromagnetic field and particle motion. These equations are discretized in time using the finite-difference scheme which are then combined to yield the Courant-condition-free, implicit equations to determine the future electromagnetic field in a large time step compared to the electron time scales. Finally, an implicit correction method to the longitudinal (curl-free) part of the electric field is described.

2.1. The Fundamental Equations of the Field and Particles

In order to realize a kinetic simulation of plasmas in large time-and-space scales, we introduce a slightly backward time-descentered scheme. The Maxwell equations are used to describe the electromagnetic field which with time level suffices are written

$$\frac{1}{c}\left(\frac{\partial \mathbf{E}}{\partial t}\right)^{n+1/2} = \nabla \times \mathbf{B}^{n+\alpha} - \frac{4\pi}{c}\mathbf{j}^{n+\alpha}, \tag{1}$$

$$\frac{1}{c}\left(\frac{\partial \mathbf{B}}{\partial t}\right)^{n+1/2} = -\nabla \times \mathbf{E}^{n+\alpha}, \tag{2}$$

$$\nabla \cdot \mathbf{E}^{n+1} = 4\pi\rho^{n+1}, \tag{3}$$

$$\nabla \cdot \mathbf{B}^{n+1} = 0. \tag{4}$$

Here, $\mathbf{E}$ and $\mathbf{B}$ are the electric and magnetic fields, respectively, c is the speed of light, and α is a decentering (implicitness) parameter to be specified later. The current density $\mathbf{j}$ and the charge density ρ are implicit quantities which are to be expressed as the functions of unknown electromagnetic fields in Section 2.3.

The equations of motion for the ions are the standard Newton–Lorentz equations except the time level of the electromagnetic field which are given by

$$\left(\frac{d\mathbf{v}_j}{dt}\right)^{n+1/2} = \frac{e_i}{m_i}\left[\mathbf{E}^{n+\alpha}(\mathbf{x}_j) + (\mathbf{v}_j^{n+1/2}/c) \times \mathbf{B}^{n+\alpha}(\mathbf{x}_j)\right], \tag{5}$$

$$\left(\frac{d\mathbf{x}_j}{dt}\right)^{n+1/2} = \mathbf{v}_j^{n+1/2}. \tag{6}$$

A choice of the identical time level $t = t^{n+\alpha}$ for the electric and magnetic fields, which properly reproduces the ponderomotive force due to electromagnetic and Alfven waves, differs from other implicit algorithms [11–13, 15, 16]. This point will be discussed in Section 7.3. By contrast, the velocity in the Lorentz term must be exactly time-centered to preserve the cyclotron motion.

For the motion of the electrons, there are two options. The first one is to use the Newton–Lorentz equations, Eqs. (5) and (6), for the ions, which allows us a fully-kinetic simulation of the plasma. However, to retain the cyclotron orbit effects such as diamagnetic drift and magnetization currents, a rather small time step $\omega_{ce}\,\Delta t \sim O(0.1)$ is required. On the contrary, we choose the second option of introducing the guiding-center approximation in order to eliminate the electron cyclotron time-scale ω_{ce}^{-1}. The equations of motion are decomposed into the parallel and perpendicular components with respect to the local magnetic field, which are given by

$$\left(\frac{dv_{\|j}}{dt}\right)^{n+1/2} = \left(\frac{-e}{m_e}\right) E_{\|}^{n+\alpha} - \left(\frac{\mu_j}{m_e}\right)\frac{\partial}{\partial x_{\|}} B^{n+\alpha} \tag{7}$$

$$\mathbf{v}_{\perp j}^{n+\alpha} = c\left(\frac{\mathbf{E}\times\mathbf{B}}{B^2}\right)^{n+\alpha} + \left\{\left(\frac{m_e c}{-eB}\right)\mathbf{b}\times\left(\frac{\mu_j}{m_e}\nabla B + v_{\|j}^2\frac{\partial \mathbf{b}}{\partial x_{\|}}\right)\right\}^{n+\alpha}, \tag{8}$$

$$\left(\frac{d\mathbf{x}_j}{dt}\right)^{n+1/2} = (\mathbf{v}_{\|j}^{n+1/2} + \mathbf{v}_{\perp j}^{n+\alpha}). \tag{9}$$

In Eq. (7), $v_{\|j}$ is a scalar velocity (sign included) along the magnetic field and $\mu_j = (\frac{1}{2}m_e v_{th,j}^2/B(\mathbf{x}_j))_{t=0}$ (=const) is the magnetic moment of the jth electron with $v_{th,j}$ being its thermal velocity. The unit vector along the magnetic field line $\mathbf{b} = (\mathbf{B}/B)$ is defined locally at each particle position. The three terms of Eq. (8) represent the $E\times B$, gradient-B and curvature drifts, respectively.

It is important to note that the time indices of each term in Eqs. (7)–(9) must be consistent with their counterparts in the Newton–Lorentz equation. For example, the time level of the perpendicular velocity in Eq. (9) should be $t = t^{n+\alpha}$. Otherwise, the electrons and ions would show different responses ($E\times B$ drift, etc.) to the low-frequency component

of the electromagnetic field. The vector "parallel" velocity in Eq. (9) is defined by

$$\mathbf{v}_{\|j}^{n+1/2} = v_{\|j}^{n+1/2}\mathbf{b}^{n+\alpha}(\mathbf{x}_j). \tag{10}$$

The parallel electric field and the differential operator are defined, respectively, by $E_{\|}^{n+\alpha} = (\mathbf{b}^{n+\alpha}\cdot\mathbf{E}^{n+\alpha})$ and $\partial/\partial x_{\|} = (\mathbf{b}^{n+\alpha}\cdot\nabla)$. (Refer to the paragraph in Section 2.2 containing Eq. (13) for the proof.)

The parameter α appearing in the Maxwell equations and the equations of motion controls the degree of numerical damping of high-frequency oscillations. The parameter α must be always larger than $\frac{1}{2}$ and in the range $\frac{1}{2} < \alpha \leqslant 1$. As will be shown in Section 3.3, the decentering of the time level in the curl terms of Eqs. (1) and (2) causes damping of high-frequency light waves. Attenuation of high-frequency electromagnetic and electrostatic waves with $\omega\,\Delta t \geqslant O(1)$ which arises from the plasma responses is accomplished by the decentering of the electric and magnetic fields in the equations of motion [7]. Since a large time step $\omega_{pe}\,\Delta t \gg 1$ is generally used, the Langmuir oscillations are eliminated. A discussion will be made in Section 3.3 about how the numerical stability and energy conservation of the simulation runs are affected by the choice of the parameter α.

As noted previously, there are two options with the equations of motion of the HIDENEK code. The guiding-center approximation also of the ion motion is a natural extension of the algorithm which may permit us simulations with a larger time step with $\omega_{ci}\,\Delta t \gg 1$. The polarization drift needs to be added to the ion momentum equation to sustain propagation of the Alfven wave. On the other hand, the guiding-center approximation breaks down when the magnetic field strength approaches zero, i.e., $\delta E_{\perp}/B \sim O(1)$, as is the case with a plasma with magnetic null points. In this situation, both the ions and electrons must be treated in a fully kinetic fashion with Eqs. (5) and (6). The algorithm for this case becomes less complicated compared to that described in this section.

2.2. The Field and Particle Equations in the Finite Difference Form

The field and particle equations given in Section 2.1 are time-discretized using the finite difference scheme. The first equation of motion for the ions is written

$$\mathbf{v}_j^{n+1} = \mathbf{v}_j^n + \Delta t\frac{e_i}{m_i}\left[\tilde{\mathbf{E}}^{n+\alpha} + (\mathbf{v}_j^{n+1/2}/c)\times\tilde{\mathbf{B}}^{n+\alpha}\right], \tag{11}$$

where Δt is a time step and the velocity is defined on the integer time level as well as the position of the particles to be mentioned later. The tilde quantity stands for the field that is evaluated at the predicted particle position $\bar{\mathbf{x}}_j$ using the linear interpolation (area-weighting) of the field value which is defined on the neighborhood grids $\mathbf{x}_g$,

$$\tilde{\mathbf{E}}(\bar{\mathbf{x}}_j) \equiv \sum_g \mathbf{E}(\mathbf{x}_g)\,S(\mathbf{x}_g - \bar{\mathbf{x}}_j). \tag{12}$$

Here, $S(\mathbf{x})$ is the weight function satisfying $\int S(\mathbf{x})\,d\mathbf{x} = 1$ which acts to connect the particle (Lagrange) and field (Eulerian) quantities. The "predicted" position to evaluate the electric and magnetic fields is the mid-point of orbits which is defined by $\bar{\mathbf{x}}_j^{n+1/2} = \mathbf{x}_j^n + \frac{1}{2}\Delta t\,\mathbf{v}_{j(0)}^{n+1/2}$, where $\mathbf{v}_{j(0)}^{n+1/2}$ is the velocity calculated by means of only the known field values at $t = t^n$. The choice of the mid-point is particularly important for the magnetic field in the Lorentz term of Eq. (11) to avoid fictitious drifts of particles. For the trapped particles, a special care might be required to predict their furture positions accurately around the turning points.

We solve Eq. (11) in terms of $\mathbf{v}_j^{n+1}$ using the interpolation $\mathbf{v}^{n+1/2} = \frac{1}{2}(\mathbf{v}^n + \mathbf{v}^{n+1})$ to obtain

$$\mathbf{v}_j^{n+1} = \mathbf{v}_j^n + \Delta t\frac{e_i}{m_i}\left\{\left(\tilde{\mathbf{E}}^{n+\alpha} + \frac{\mathbf{v}_j^n}{c}\times\tilde{\mathbf{B}}^{n+\alpha}\right) + \Theta^2\tilde{\mathbf{E}}_{\|}^{n+\alpha} + \Theta\left(\tilde{\mathbf{E}}^{n+\alpha} + \frac{\mathbf{v}_j^n}{c}\times\mathbf{B}^{n+\alpha}\right)\times\tilde{\mathbf{b}}^{n+\alpha}\right\}\Big/(1+\Theta^2), \tag{13}$$

$$\mathbf{x}_j^{n+1} = \mathbf{x}_j^n + \Delta t\,\mathbf{v}_j^{n+1/2}, \tag{14}$$

where $\tilde{\mathbf{E}}_{\|}^{n+\alpha} = (\tilde{\mathbf{E}}^{n+\alpha}\cdot\tilde{\mathbf{b}}^{n+\alpha})\,\tilde{\mathbf{b}}^{n+\alpha}$, $\Theta(\mathbf{x}) = \frac{1}{2}\Delta t(e_i/m_i c)\,|\tilde{\mathbf{B}}|^{n+\alpha}$. It is mentioned in passing that the first term in the right-hand side of Eq. (13), $\mathbf{v}_j^n$, has been intentionally separated out of the denominator $(1+\Theta^2)$ which includes the future magnetic field $\mathbf{B}^{n+\alpha}$. In the $|\Theta| \gg 1$ limit which corresponds to the guiding-center approximation, the first-order terms yield

$$\mathbf{v}_j^{n+1} \cong \mathbf{v}_j^n + \Delta t\frac{e_j}{m_j}\left\{\tilde{\mathbf{E}}_{\|}^{n+\alpha} + \frac{1}{\Theta}\left(\tilde{\mathbf{E}}^{n+\alpha} + \frac{\mathbf{v}_j^n}{c}\times\tilde{\mathbf{B}}^{n+\alpha}\right)\times\tilde{\mathbf{b}}^{n+\alpha}\right\}. \tag{15}$$

Decomposition of the parallel and perpendicular components in terms of the direction of the magnetic field $\mathbf{b}^{n+\alpha}$ gives

$$\mathbf{v}_{\perp j}^{n+1} \cong c\tilde{\mathbf{E}}^{n+\alpha}\times\tilde{\mathbf{b}}^{n+\alpha}/B^{n+\alpha} \tag{16}$$

$$v_{\|j}^{n+1} \cong v_{\|j}^n + \Delta t\frac{e_j}{m_j}(\tilde{\mathbf{E}}^{n+\alpha}\cdot\tilde{\mathbf{b}}^{n+\alpha}). \tag{17}$$

These are obviously the leading terms of the guiding-center equations of motion Eqs. (7)–(8).

The equations of motion for the electrons Eqs. (7)–(9) are similarly discretized in time and are given by

$$v_{\|j}^{n+1} = v_{\|j}^{n} + \Delta t \left(\left(\frac{-e}{m_e} \right) \tilde{E}_{\|}^{n+\alpha} - \left(\frac{\mu_j}{m_e} \right) \frac{\partial}{\partial x_{\|}} \tilde{B}^{n+\alpha} \right), \tag{18}$$

$$\mathbf{x}_j^{n+1} = \mathbf{x}_j^{n} + \Delta t \left\{ \mathbf{v}_{\|j}^{n+1/2} + \mathbf{v}_{\perp j}^{n+\alpha}(\bar{\mathbf{x}}_j^{n+1/2}) \right\}. \tag{19}$$

The perpendicular velocity is a function of the future electromagnetic field as specified by Eq. (8), and the direction of the parallel velocity is defined with respect to $\mathbf{b}^{n+\alpha}$ by Eq. (10).

The Maxwell equations are discretized with respect to time and are written

$$\mathbf{E}^{n+1} - \mathbf{E}^{n} = c\,\Delta t\, \nabla \times \mathbf{B}^{n+\alpha} - 4\pi\,\Delta t\, \mathbf{j}^{n+\alpha}, \tag{20}$$

$$\mathbf{B}^{n+1} - \mathbf{B}^{n} = -c\,\Delta t\, \nabla \times \mathbf{E}^{n+\alpha}. \tag{21}$$

In order to avoid the Courant condition which severely restricts magnitude of the time step against the given space grid intervals, we eliminate $\mathbf{B}^{n+1}$ from Eqs. (20) and (21) to derive an implicit equation for $\mathbf{E}^{n+1}$. During this algebra, we use for $\mathbf{E}^{n+\alpha}$ the linear interpolation of the field quantity to the non-integer time level

$$\mathbf{E}^{n+\alpha} = \alpha \mathbf{E}^{n+1} + (1-\alpha)\,\mathbf{E}^{n}, \tag{22}$$

and a similar interpolation for $\mathbf{B}^{n+\alpha}$. This procedure yields the equation to determine the future electric field $\mathbf{E}^{n+1}$,

$$\begin{aligned} &[1 + (\alpha c\,\Delta t)^2\, \nabla \times \nabla \times]\, \mathbf{E}^{n+1} \\ &\quad = [1 - \alpha(1-\alpha)(c\,\Delta t)^2\, \nabla \times \nabla \times]\, \mathbf{E}^{n} \\ &\qquad + c\,\Delta t\, \nabla \times \mathbf{B}^{n} - 4\pi\,\Delta t\, \mathbf{j}^{n+\alpha}. \end{aligned} \tag{23}$$

Here, the $\nabla \times \mathbf{B}^{n+\alpha}$ term has been split to the $\nabla \times \mathbf{B}^{n}$ term and the $\nabla \times \nabla \times \mathbf{E}$ terms which appear on the both sides of Eq. (23). The functional form of the current density in the right-hand side of the equation is to be specified in Section 2.3. The future magnetic field is obtained using Eq. (21) once $\mathbf{E}^{n+1}$ has been known.

It is noted that, since the inequality $(c\,\Delta t/\lambda)^2 \gg 1$ holds ($\nabla \times \approx 1/\lambda$), Eq. (23) is essentially decomposed into the magnetic component $\nabla \times \mathbf{B}^{n+\alpha} = (4\pi/c)\,\mathbf{j}_{\mathrm{T}}^{n+\alpha}$ and the electrostatic component $\mathbf{E}_{\mathrm{L}}^{n+1} = \mathbf{E}_{\mathrm{L}}^{n} - 4\pi\,\Delta t\,\mathbf{j}_{\mathrm{L}}^{n+\alpha}$, where T and L denote the transverse (divergence-free) and longitudinal (curl-free) parts, respectively. The latter equation is equivalently transformed into the continuity equation $(\rho^{n+1} - \rho^{n})/\Delta t + \nabla \cdot \mathbf{j}_{\mathrm{L}}^{n+\alpha} = 0$ by using Eq. (3). A deviation of this longitudinal electric field from the true electric field obtained by $\nabla \cdot \mathbf{E}^{n+1} = 4\pi\rho^{n+1}$ will be adjusted later. As has been instructed here, the unity terms in the square brackets make a significant contribution to the electrostatic part and cannot be ignored. Despite the simplicity of the decomposed equations, however, we do not use them in the simulation. The reason against the decomposed equations is that the above magnetoinductive (Darwin) algorithm requires a complete separation of the transverse current $\mathbf{j}_{\mathrm{T}}$ ($\nabla \cdot \mathbf{j}_{\mathrm{T}} = 0$) from the longitudinal current $\mathbf{j}_{\mathrm{L}}$ ($\nabla \times \mathbf{j}_{\mathrm{L}} = 0$). This is a non-trivial operation in the real-space and for the implicit current density given in the next subsection; an incomplete decomposition of the current components leads to poor accuracy and numerical instability.

2.3. The Closely-Coupled Field-Particle Equations

a. *The Time-Implicit Equations for the Electromagnetic Field*

To obtain the future electromagnetic field by Eq. (23), the current density must be specified to have a closure of the equation. A prediction of the current density in the Maxwell equations is the key of the implicit algorithm which must be nonlinearly stable against a large time step. (A prediction without suppression of the high-frequency plasma oscillations may fail for $\omega_{pe}\,\Delta t \geqslant 2$.) In the present algorithm, the current density is directly expressed in terms of the future electromagnetic field with the aid of the equations of motion:

$$\begin{aligned} \mathbf{j}^{n+\alpha}(\mathbf{x}) &= \sum_j e_j \mathbf{v}_j^{n+\alpha} S(\mathbf{x} - \tilde{\mathbf{x}}_j^{n+\alpha}) \\ &= \sum_{j=i} e_i \Bigg[\mathbf{v}_j^{n} + \alpha\,\Delta t \frac{e_i}{m_i} \Bigg\{ \left(\tilde{\mathbf{E}}^{n+\alpha} + \frac{\mathbf{v}_j^{n}}{c} \times \tilde{\mathbf{B}}^{n+\alpha} \right) \\ &\quad + \Theta^2 \tilde{\mathbf{E}}_{\|}^{n+\alpha} + \Theta \left(\tilde{\mathbf{E}}^{n+\alpha} + \frac{\mathbf{v}_j^{n}}{c} \times \tilde{\mathbf{B}}^{n+\alpha} \right) \\ &\quad \times \tilde{\mathbf{b}}^{n+\alpha} \Bigg\} \Big/ (1+\Theta^2) \Bigg] S(\mathbf{x} - \bar{\mathbf{x}}_j^{n+\alpha}) \\ &\quad + \sum_{j=e} (-e) \Bigg[\Bigg\{ v_{\|j}^{n} + \alpha\,\Delta t \left(\left(\frac{-e}{m_e} \right) \tilde{E}_{\|}^{n+\alpha} \\ &\quad - \left(\frac{\mu_j}{m_e} \right) \frac{\partial}{\partial x_{\|}} \tilde{B}^{n+\alpha} \right) \Bigg\} \tilde{\mathbf{b}}^{n+\alpha} \\ &\quad + \tilde{\mathbf{v}}_{\perp j}^{n+\alpha}(\bar{\mathbf{x}}_j^{n+1/2}) \Bigg] S(\mathbf{x} - \bar{\mathbf{x}}_j^{n+\alpha}) \\ &\quad - c \nabla \times \sum_{j=e} \mu_j \tilde{\mathbf{b}}^{n+\alpha} S(\mathbf{x} - \bar{\mathbf{x}}_j^{n+\alpha}), \end{aligned} \tag{24}$$

where $\Theta(\mathbf{x}) = \frac{1}{2}\,\Delta t\,(e_i/m_i c)\,|\mathbf{B}|^{n+\alpha}$ and $\mathbf{v}_{\perp j}^{n+\alpha}$ is given by Eq. (8). The last term of Eq. (24) accounts for the magnetization current $\mathbf{j}_M = -c \nabla \times (p_{\perp}^{(e)} \mathbf{b}/B)$ of the electrons under the guiding-center approximation. The symbols

$\sum_{j=i}$ and $\sum_{j=e}$ denote summations over the ion and electron species, respectively. As before, the electromagnetic field with the tilde is evaluated with the weighting scheme Eq. (12). The time level of $\tilde{\mathbf{v}}_{\perp j}$ should be again $t = t^{n+\alpha}$ to be consistent with the ion cross-field response. The basic unknown quantities in the right-hand side of Eq. (24) are $\mathbf{E}^{n+1}$ and $\mathbf{B}^{n+1}$.

Substitution of the implicitly expressed current density Eq. (24) into Eq. (23) yields the matrix equation to determine the future electric field $\mathbf{E}^{n+1}$,

$$A_v \mathbf{E}^{n+1} = \mathbf{S}_p(\mathbf{E}^n, \mathbf{B}^n; \mathbf{E}^{n+1}, \mathbf{B}^{n+1}). \tag{25}$$

The matrix A_v on the left-hand side represents a vacuum response which is defined by

$$A_v = \mathbf{1} + (\alpha c\, \Delta t)^2 (\nabla\nabla - \mathbf{1}\nabla^2), \tag{26}$$

and the source vector $\mathbf{S}_p$ on the right-hand side is given by

$$\begin{aligned}\mathbf{S}_p = {} & [1 - \alpha(1-\alpha)(c\,\Delta t)^2 (\nabla\nabla - \nabla^2)]\, \mathbf{E}^n \\ & + c\,\Delta t\, \nabla \times \mathbf{B}^n - 4\pi\, \Delta t \\ & \times \left\{ \sum_{j=i} e_i \left[\mathbf{v}_j^n + \alpha\, \Delta t\, (e_i/m_i) \left(\tilde{\mathbf{E}}^{n+\alpha} + \frac{\mathbf{v}_j^n}{c} \times \tilde{\mathbf{B}}^{n+\alpha} \right) \right. \right. \\ & \left. \left. \div (1 + \Theta^2) \right] S(\mathbf{x} - \bar{\mathbf{x}}_j^{n+\alpha}) + \cdots \right\}. \end{aligned} \tag{27}$$

The symbol $\nabla\nabla$ denotes a dyadic operator and $\mathbf{1}$ the unit tensor. (Refer to Section 3.1 for further modifications of the above equations.) Equations (25)–(27) and (21) constitute a closed set of the Courant-condition-free, implicit equations to determine the future electromagnetic field. These equations are named "closely-coupled field-particle (CCFP) equations" after their nature of nonlinear coupling of the fields and particles.

b. *A Correction to the Longitudinal Electric Field*

The third and fourth Maxwell equations, Eqs. (3) and (4), are the conditions to determine the initial value of the electromagnetic field and they need not be used mathematically for $t > 0$. However, it is well known that a discreteness of the space grids which are commonly used in the simulation introduces a small but finite error to the area-weighted current density equation (24). The error occurs in such a way that the current density thus obtained does not satisfy the continuity equation with good accuracy, or equivalently, Gauss's law [22]. Hence, a correction to the longitudinal (curl-free) part of the area-weighted current density is required in each time step.

Strictly speaking, a small deviation in the longitudinal part of the current density affects both the longitudinal and transverse (divergence-free) parts of the electric field in the implicit algorithm. However, except for a sharp gradient region in a plasma, the deviation affects only the longitudinal electric field. Thus, the longitudinal electric field is corrected afterwards using the Gauss's law (3) and the expansion method described in Ref. [23]. This correction method is verified since a cross talk between the longitudinal and transverse components of the electric field, which occurs through the implicit current density, is by orders of magnitude small compared to non-cross talk terms when the plasma density and magnetic field are varying slowly. A similar correction method was used in the direct implicit method [15, 16] and the previous version of the closely-coupled implicit method [7].

For the correction of the longitudinal electric field, we express the true electric field $\mathbf{E}^{n+1}$ as a sum of the electric field before the correction $\check{\mathbf{E}}^{n+1}$ (the solution of Eq. (25)) and the longitudinal correction which is a gradient of the scalar function $\delta\varphi$,

$$\mathbf{E}^{n+1} = \check{\mathbf{E}}^{n+1} - \nabla\, \delta\varphi. \tag{28}$$

Substitution of Eq. (28) into Gauss's law (3) yields the equation to determine $\delta\varphi$,

$$-\nabla^2 \delta\varphi = 4\pi\rho^{n+1} - \nabla \cdot \check{\mathbf{E}}^{n+1}. \tag{29}$$

Again, the charge density ρ^{n+1}, which is not known at this moment, needs to be obtained in an implicit fashion to realize a large time step simulation. For this purpose, the charge density is Taylor-expanded in terms of a small displacement due to the correction electric field $\nabla\delta\varphi$ and the vector identity is used [23]

$$\begin{aligned}\rho^{n+1}(\mathbf{x}) &= \sum_j e_j S(\mathbf{x} - \mathbf{x}_j^{n+1}) \\ &\cong \sum_j e_j S(\mathbf{x} - \mathbf{x}_{j(I)}^{n+1}) - \nabla \cdot \left(\sum_j e_j \delta\mathbf{x}_j S(\mathbf{x} - \mathbf{x}_{j(I)}^{n+1}) \right). \end{aligned} \tag{30}$$

The displacement is defined by $\delta\mathbf{x}_j = \mathbf{x}_j^{n+1} - \mathbf{x}_{j(I)}^{n+1}$ with $\mathbf{x}_j^{n+1}$ being the true particle position at $t = t^{n+1}$ and $\mathbf{x}_{j(I)}^{n+1}$ being the position calculated using the already known electromagnetic field $\check{\mathbf{E}}^{n+1}$ and $\mathbf{B}^{n+1}$. The displacement of the ions, for example, is calculated to be

$$\begin{aligned}\delta\mathbf{x}_j^{(i)} = -\frac{1}{2}\alpha(\Delta t)^2 \frac{e_i}{m_i} \{ & \nabla\delta\varphi + \nabla\delta\varphi \times \Theta\mathbf{b}^{n+\alpha} \\ & + \Theta^2 \nabla_{\parallel}\delta\varphi \}/(1 + \Theta^2), \end{aligned} \tag{31}$$

where the vector operator is defined by $\nabla_{\parallel} = \mathbf{b}^{n+\alpha}(\mathbf{b}^{n+\alpha} \cdot \nabla)$.

Since the final magnetic field has already been determined, together with $\check{\mathbf{E}}^{n+1}$, at this stage, the displacement $\delta\mathbf{x}_j$, hence, the charge density ρ^{n+1}, is solely a function of $\delta\varphi$. By substituting Eq. (30) into Eq. (29) and shifting the $\delta\varphi$-dependent terms to the left-hand side, we obtain a completely implicit equation to determine the correction scalar potential $\delta\varphi$,

$$\begin{aligned}\nabla^2\delta\varphi + \tfrac{1}{2}\alpha(\Delta t)^2\nabla\cdot(\omega_{pi}^2(\mathbf{x})\{\nabla\delta\varphi + \Theta^2\nabla_{\|}\delta\varphi \\ + \Theta\nabla\delta\varphi\times\mathbf{b}\}/(1+\Theta^2) \\ + \omega_{pe}^2(\mathbf{x})\nabla_{\|}\delta\varphi) + 4\pi(-e)c\alpha\Delta t\nabla \\ \cdot(\nabla\delta\varphi\times(\mathbf{b}/B)n_e(\mathbf{x})) \\ = -4\pi\bar{\rho}^{n+1} + \nabla\cdot\check{\mathbf{E}}^{n+1}. \qquad (32)\end{aligned}$$

Here, the zeroth order charge density is defined by $\bar{\rho}^{n+1}(\mathbf{x}) = \sum_j e_j S(\mathbf{x} - \mathbf{x}_{j(l)}^{n+1})$ and $\omega_{pj}^2(\mathbf{x}) = 4\pi n_j(\mathbf{x})\, e_j^2/m_j$. It should be noted in Eq. (32) that the vacuum response is mostly shielded by the plasma dielectric response. The ratio of the plasma response to that of the vacuum is approximated by $\frac{1}{2}\alpha(\Delta t)^2\ (\omega_{pi}^2(\mathbf{x}) + b_{\|}\omega_{pe}^2(\mathbf{x}))$ which is much greater than unity in the plasma, due to $\omega_{pe}^{(0)}\Delta t \gg 1$.

The procedures of the simulation using the method described here are summarized in the Appendix. The particle ions and electrons are first generated in the Cartesian $(\mathbf{x}, \mathbf{v})$ space. After collecting the current and charge densities, $\mathbf{j}^{(0)}$ and $\rho^{(0)}$, the initial electromagnetic field is determined. Using this magnetic field, the electron velocity is converted from the Cartesian to $(\mu, v_{\perp}, v_{\|})$ representations. Then, a time cycle of the simulation begins. First, the current density $\mathbf{j}$ and the charge densities of the ions and electrons ρ_i, ρ_e are summed over particles. The electromagnetic field $\check{\mathbf{E}}^{n+1}$ and $\mathbf{B}^{n+1}$ are solved using the CCFP equation, Eq. (25), and Eq. (21). Next, the charge densities at time $t = t^{n+1}$ are summed to make the correction to the longitudinal part of the electric field using Eq. (32). Finally, the velocity and position of all the particles are advanced by a full time step to proceed to the new time cycle.

3. NUMERICAL METHODS FOR THE IMPLICITLY COUPLED EQUATIONS

Following the description of the implicit simulation algorithm in Section 2, this section gives a key approximation and guidelines of the numerical techniques which facilitate solution of the coupled field-particle equations. Dependence of energy conservation of the simulation on the implicitness parameter is also discussed.

3.1. A Key Approximation in the CCFP Equations

Here, we present an important and accuracy-preserving approximation which makes the solution of the CCFP equations possible under the limited computing resources. As have been described in Section 2, the implicit current and charge densities, Eqs. (24) and (30), consist of summations over the particles with the unknown electromagnetic field being involved. Calculation of these terms, which represent a coupling of the adjacent plasma elements through the electromagnetic field, becomes inhibitedly expensive unless the following approximation is introduced to these coupling terms:

$$\sum_j f_j\tilde{\mathbf{E}}^{n+\alpha}(\mathbf{x}_j)\, S(\mathbf{x}-\mathbf{x}_j)$$

$$= \sum_j f_j\{\alpha(\tilde{\mathbf{E}}^{n+1}(\mathbf{x}_j) - \tilde{\mathbf{E}}_1(\mathbf{x}_j)) + \tilde{\mathbf{E}}_0(\mathbf{x}_j)\}\, S(\mathbf{x}-\mathbf{x}_j) \qquad (33)$$

$$\cong \alpha F(\mathbf{x})(\mathbf{E}^{n+1}(\mathbf{x}) - \mathbf{E}_1(\mathbf{x})) + \sum_j f_j\tilde{\mathbf{E}}_0(\mathbf{x}_j)\, S(\mathbf{x}-\mathbf{x}_j), \qquad (34)$$

where $\mathbf{E}_1$ is a quantity which well approximates $\mathbf{E}^{n+1}$ and $\mathbf{E}_0 = \alpha\mathbf{E}_1 + (1-\alpha)\mathbf{E}^n$. The linear interpolation Eq. (22) has been used in the equality of Eq. (33). Note that $(\mathbf{E}^{n+1} - \mathbf{E}_1)$ is paired in Eq. (34) to minimize an error associated with this approximation and that the tilde is removed from this term. The summation of f_j over the particles becomes $F(\mathbf{x}) = \sum_j f_j S(\mathbf{x}-\mathbf{x}_j)$. Thus, the unknown electromagnetic field is separated out of the summation over the particles. Using this approximation, Eqs. (25)–(27) given in Section 2.3(a) are rewritten

$$A(n_i, n_e; \mathbf{B}^{n+1})\,\mathbf{E}^{n+1} = \mathbf{S}(\mathbf{E}^n, \mathbf{B}^n; \mathbf{B}^{n+1}). \qquad (35)$$

Here, the matrix A comprises both the plasma and vacuum terms as defined by

$$\begin{aligned}A &= \mathbf{1} + (\alpha c\,\Delta t)^2(\nabla\nabla - \mathbf{1}\nabla^2) + D \\ D &= (\alpha\Delta t)^2[\omega_{pi}^2(\mathbf{x})\{\mathbf{1} - \Theta\mathbf{b}^{n+\alpha}\times\mathbf{1} \\ &\quad + \Theta^2(\mathbf{bb})^{n+\alpha}\}/(1+\Theta^2) + \omega_{pe}^2(\mathbf{x})(\mathbf{bb})^{n+\alpha}] \\ &\quad - 4\pi(-e)c\alpha\Delta t(n_e(\mathbf{x})/B)\,\mathbf{b}^{n+\alpha}\times\mathbf{1}, \qquad (36)\end{aligned}$$

where $(\mathbf{bb})$ is a dyadic tensor and $\omega_{pj}^2(\mathbf{x})$ which is proportional to charge density ρ_j can be highly space-dependent. The unknown electric field $\mathbf{E}^{n+1}$ has been removed from $\mathbf{S}_p$ to obtain the new source vector

$$\begin{aligned}\mathbf{S} &= [1 - \alpha(1-\alpha)(c\,\Delta t)^2(\nabla\nabla - \nabla^2)] \\ &\quad \times\mathbf{E}^n + c\,\Delta t\,\nabla\times\mathbf{B}^n + D\mathbf{E}_1 - 4\pi\,\Delta t \\ &\quad \times\left\{\sum_{j=i} e_i\left[\mathbf{v}_j^n + \alpha\,\Delta t(e_i/m_i)\left(\tilde{\mathbf{E}}_0 + \frac{\mathbf{v}_j^n}{c}\times\tilde{\mathbf{B}}^{n+\alpha}\right)\right.\right. \\ &\quad \left.\left. \div(1+\Theta^2)\right] S(\mathbf{x} - \bar{\mathbf{x}}_j^{n+\alpha}) + \cdots\right\}. \qquad (37)\end{aligned}$$

As $\mathbf{E}_1$ we often use the electric field of the last time step. When $\mathbf{E}_1$ is chosen independently of the iteration for solving the coupled field-particle equations, the summations in Eq. (37) need to be calculated only once before the commencement of the iteration.

It is extremely important to note with the aforementioned approximation, that a major contribution to the summation $\sum f_j \tilde{\mathbf{E}}^{n+\alpha} S(\mathbf{x}-\mathbf{x}_j)$ is contained in the second term of Eq. (34) for which the double summation is taken "accurately" while preserving the kinetic flavor of the original equations. The first summation is taken to calculate $\tilde{\mathbf{E}}(\mathbf{x}_j)$ using Eq. (12) and the second summation to obtain $\sum_j f_j \tilde{\mathbf{E}}(\mathbf{x}_j)\, S(\mathbf{x}-\mathbf{x}_j)$. The accuracy of this approximation was numerically proved in the previous literature for the thermal eigenmodes in the 2D magnetized plasma and for the kinetic Alfven wave in the finite temperature plasma [7]. The present approximation greatly contributes to minimize a degradation of energy conservation. By constrast, a simpler but less accurate approximation, i.e., $\sum_j f_j \tilde{\mathbf{E}}^{n+\alpha}(\mathbf{x}_j)\, S(\mathbf{x}-\mathbf{x}_j) \cong F(\mathbf{x})\, \mathbf{E}^{n+\alpha}$ has been tested in the application to be shown in Section 4. However, the latter approximation results in a rapid and monotonic decrease in the kinetic energy, especially that of the electrons. The loss of the kinetic energy may be attributed to the totally fluid-like treatment which eliminates a kinetic coupling in the plasma.

3.2. The Solution of the CCFP Equations

It has been shown in Section 3.1 that the CCFP equations are cast in the form of an implicit matrix equation:

$$A\Psi = S(\Psi). \tag{38}$$

Here, Ψ is an unknown column vector representing the electric field to be solved, A is the matrix which includes both the plasma response and vacuum terms ($\nabla \times \nabla \times$), and S the source vector. Since the source S depends on Ψ nonlinearly due to the choice of the magnetic field at the intermediate time level, we need to use an iterative method for the solution of the matrix equation (38). In fact, $\mathbf{E}^{n+\alpha} \times \mathbf{B}^{n+\alpha}$ term, for example, depends on $\mathbf{E}^{n+1}$ quadratically since $\mathbf{B}^{n+1}$ is a function of $\mathbf{E}^{n+1}$.

The method that we adapt to the solution of the nonlinear equation Eq. (38) is a relaxation method. First, all the Ψ-linear terms in $S(\Psi)$ are shifted to the left-hand side to treat the equation as implicitly as possible,

$$L\Psi = Q(\Psi). \tag{39}$$

This equation is solved to obtain $\Psi^{(+)} = L^{-1}Q(\Psi^{(r)})$ by assuming that $Q(\Psi)$ is known. The superscript (r) denotes the last cycle of the iteration. The new value of the $(r+1)$th cycle is given in a Newton–Raphson manner,

$$\Psi^{(r+1)} = \varepsilon \Psi^{(+)} + (1-\varepsilon)\, \Psi^{(r)} \qquad (0 < \varepsilon \leqslant 1). \tag{40}$$

The new value $\Psi^{(r+1)}$ is then back-substituted to $Q(\Psi)$ in the right-hand side of Eq. (39), and the iteration is resumed until a relative variation of the norm $|\Psi|$ becomes smaller than a given tolerance. When the Ψ-nonlinearity of Q is not so strong, $\varepsilon = 1$ can be used in Eq. (40). However, even when the Ψ-nonlinearity is weak, the back-substitution must be executed at least once and Eq. (39) must be solved twice; in the first cycle of the iteration, the unknown $\mathbf{B}^{n+1}$ is being replaced by $\mathbf{B}^n$ in Eq. (25).

In order to take an advantage of the implicit algorithm, i.e., to be free from the Courant condition, the above iteration must be repeated several times to ensure that physical informations propagate in space to adjust themselves. If we start from a good initial guess which is usually the field value of the last time step, only a few iteration cycles are required before Eq. (38) converges. Actually, in one dimension the solution of Eq. (38) requires only a few (typically four) iteration cycles before the iteration converges for the tolerance of 10^{-5}.

Concerning the solution of the core equation (39), several methods have been tested to invert the matrix L. Experiences imply that an accurate solution of the core equation is essential to the nonlinear iteration described here. In the one-dimensional case, the Gaussian elimination method has been successfully applied since the matrix L is a sparse band-matrix connecting the quantities of the spatially adjacent grids [24]. However, in three dimensions with $N_x \times N_y \times N_z$ grids, the matrix L becomes a huge band matrix whose column size is of the order of $(N_x N_y N_z)$. This makes the Gaussian elimination method impractical to use for reasons of memory and accuracy. Alternatively at first, an iterative method was applied to Eq. (39), where only the diagonal terms were retained in the left-hand side to solve the equation and the new solution was back-substituted to the right-hand side of the equation. This iteration for the core equation converged, but energy conservation degraded eventually in the simulation because the nonlinear Ψ-iteration was affected by the inaccuracy of the core equation solution.

In order to eliminate the aforementioned difficulty encountered in the solution of the core equation (39), the bi-conjugate gradient (BCG) method [25] has been introduced. In the BCG matrix solver, a recursive solution converges steadily to the final solution which is to be obtained in a finite number of iterations. Practically, a convergence of the BCG solver depends on the method of preconditioning the original matrix. A *block-type* BCG solver prescribes the 3×3 *core matrix* elements simultaneously as a block; the core matrix corresponds to the diagonal element $\Psi_{ijk} = (E_x, E_y, E_z)_{ijk}$. On the other hand, a *scalar-type* solver preconditions each row of the matrix separately. The block-type solver converges much faster than the scalar-type one when the skewed symmetric elements of the core matrix which arise from the $\mathbf{E} \times \mathbf{B}$ drift are predominant over the

diagonal elements. The accuracy of the solution obtained by the BCG method is quite satisfactory, and therefore, the reliability of the nonlinear Ψ-iteration and the simulation itself have improved dramatically (Section 6).

For the solution of the closely-coupled field-particle equations, the real (configuration) space is used in the present implicit method (HIDENEK). This is because the matrix L of the CCFP equations in Eq. (39) is highly space-dependent and the Fourier-decomposed left-hand side $\mathrm{FFT}^{-1}\{L\Psi\}$ becomes a convolution of almost all the Fourier modes for the inhomogeneous plasma simulation. This is particularly the case in the application of Section 6, where a large helical perturbation takes place in the plasma density and the magnetic field structure, in association with the kink instability. In real space, by contrast, the matrix L causes a coupling of only three points in the one-dimensional case and 27 ($=3^3$) or less adjacent grid quantities in the three-dimensional simulation. Therefore, the present implicit algorithm prefers to treat the spatial localization and inhomogeneity of the phenomena in real space; even for a weakly inhomogeneous plasma, the iteration of the CCFP equation converges more rapidly in real space.

To spatially discretize the closely-coupled field-particle equations, a unique set of the non-staggered space grids is used. The choice against the staggered (interleaved) grids is that they make the boundary conditions and coding of the CCFP equations quite complicated in three-dimensions which results in the less-sparse band matrix L in Eq. (39). With the non-staggered grids, all the particle informations are accumulated to the same non-staggered grids on which all the electromagnetic fields are calculated. The center-differential scheme is used for the spatial derivatives so that their mid-points are centered with respect to the non-derivative terms in the field equations. The spatial derivatives have second-order accuracy in space.

The normalization of physical quantities to be adopted in the applications of Sections 4–6 is related to the electromagnetic waves [31]. This consists of four basic units, the length: c/ω_{pe}, time: ω_{pe}^{-1}, mass: m_e and the electronic charge: e (absolute value). The ($\hat{}$) quantities are normalized quantities which are used in the simulation:

$$\hat{x}=\frac{x}{c/\omega_{pe}},\quad \hat{t}=\omega_{pe}t,\quad \hat{m}_j=\frac{m_j}{m_e},\quad \hat{e}_j=\frac{e_j}{e}. \tag{41}$$

Other quantities such as the velocity, frequency, and electromagnetic fields are normalized by combining these basic units:

$$\hat{\mathbf{v}}=\frac{\mathbf{v}}{c},\quad \hat{\omega}=\frac{\omega}{\omega_{pe}},\quad \hat{\mathbf{E}}=\frac{e\mathbf{E}}{m_e c\omega_{pe}},\quad \hat{\mathbf{B}}=\frac{e\mathbf{B}}{m_e c\omega_{pe}}. \tag{42}$$

With this normalization, the constant in the field equations is transformed as $(4\pi)\to(1/n_0)$ and the light speed (c) disappears everywhere (n_0: the average particle number density per unit-length cube).

3.3. A Choice of the Time-Decentering Parameter and Energy Conservation

The implicitness parameter α which appears in the equations of motion and the CCFP equations must be in the range of $\frac{1}{2}<\alpha\leqslant 1$ to damp out high-frequency electrostatic and electromagnetic oscillations numerically. The proof of the high-frequency wave damping in [7, Section 3] applies to the present HIDENEK algorithm. Here, we will show the stability and energy conservation of the present algorithm, especially, against the electromagnetic waves and the electron $E\times B$ drift.

First, we focus on the electromagnetic response of the algorithm and prove its numerical stability against electromagnetic waves. Since the fast (electron) time scale is considered in this analysis, the ions are assumed immobile and only the electron current is taken into account: $\mathbf{j}_e^{n+\alpha}=(-e)\,n_0 c\mathbf{E}^{n+\alpha}\times\mathbf{B}_0/B_0^2$. For the monochromatic plane wave $\mathbf{E}$, $\mathbf{B}=\mathbf{E}_k$, $\mathbf{B}_k\times\exp[i(\mathbf{k}\cdot\mathbf{x}-\omega t)]$, we have

$$\begin{aligned}-i\omega\,\Delta t\,\mathbf{E}^{n+1/2}&=\{ic\,\Delta t\,\mathbf{k}\times\mathbf{B}^{n+1/2}\\&\quad-\Omega_B\,\Delta t\,\mathbf{E}^{n+1/2}\times\mathbf{b}_0\}\\&\quad\times\exp(-i(\alpha-\tfrac{1}{2})\,\omega\,\Delta t),\\-i\omega\,\Delta t\,\mathbf{B}^{n+1/2}&=-ic\,\Delta t\,\mathbf{k}\times\mathbf{E}^{n+1/2}\\&\quad\times\exp(-i(\alpha-\tfrac{1}{2})\,\omega\,\Delta t),\end{aligned} \tag{43}$$

where $\Omega_B=4\pi c(-e)\,n_0/B_0=\omega_{pe}^2/\omega_{ce}$. Eliminating $\mathbf{B}^{n+1/2}$ from Eqs. (43) and equating the determinant with zero, we obtain the dispersion equation

$$\left(1-\left(\frac{ck}{\omega}\right)^2\exp\left(-2i\left(\alpha-\frac{1}{2}\right)\omega\,\Delta t\right)\right)\pm\frac{\Omega_B}{\omega}\exp\left(-i\left(\alpha-\frac{1}{2}\right)\omega\,\Delta t\right)=0. \tag{44}$$

In the vacuum ($\Omega_B=0$), we obtain the frequency $\omega_r\cong\pm ck$ and the growth rate $\omega_i\cong-ck(\alpha-\frac{1}{2})\,\omega\,\Delta t$. The choice of $\alpha>\frac{1}{2}$ damps the light waves. In the plasma, the solution to Eq. (44) for the long wavelength limit $\Omega_B\gg ck$ (i.e., $\omega_{pe}/\omega_{ce}\gg ck/\omega_{pe}$), becomes

$$\begin{aligned}\omega_r&\cong\pm\Omega_B\\\omega_i&\cong-(\alpha-\tfrac{1}{2})(\Omega_B^2+(ck)^2)\,\Delta t.\end{aligned} \tag{45}$$

Unfortunately, this solution applies only for $|\Omega_B|\,\Delta t\ll 1$. Thus, a numerical solution of Eq. (44) is made for $\omega_{pe}/\omega_{ce}=1$, $\alpha=0.6$, and $\omega_{pe}\,\Delta t=100$ (the parameters

used in Section 6). The imaginary part of the frequency becomes negative, which starts with $\omega_i/\omega_{pe} \cong -5.8 \times 10^{-3}$ at $ck/\omega_{pe} = 0$. The magnitude of the damping rate increases with the wavenumber and we have $\omega/\omega_{pe} \cong 0.95 - 5.3 \times 10^{-2} i$ at $ck/\omega_{pe} = 1$. For $\alpha > \frac{1}{2}$, the algorithm becomes stable both against the light waves and electron $E \times B$ drift current $\mathbf{j}_{\perp e}^{n+\alpha}$ in the plasma.

Next, we will show the dependence of the energy conservation on the decentering parameter α. In this analysis we use the following definition as the change in the system total energy,

$$\Delta W_{\text{tot}} = \Delta W_F + \sum_s \Delta W_{K,s}. \tag{46}$$

The change in the kinetic energies of the ion and electron species, respectively, is calculated to be

$$\Delta W_{K,i} = \Delta t \int \mathbf{E}^{n+\alpha} \cdot \mathbf{j}_i^{n+1/2} \, d\mathbf{x}, \tag{50}$$

$$\Delta W_{K,e} \cong \Delta t \int \mathbf{E}_{||}^{n+\alpha} \cdot \mathbf{j}_{||e}^{n+1/2} \, d\mathbf{x} + \sum_{j=e} \tfrac{1}{2} m_e \{(v_{\perp j}^{n+1})^2 - (v_{\perp j}^n)^2\}. \tag{51}$$

The electron kinetic energy does not change in association with the $-\mu_j \nabla_{||} B$ force because the energy is internally transferred between the parallel and perpendicular components. Thus, the change in the system total energy is given

Here, $\frac{1}{2}m_e\mathbf{v}_j^2 = \frac{1}{2}m_e(v_{\|j}^2 + \mathbf{v}_{\perp j}^2) + \mu_j B(\mathbf{x}_j)$ for the electrons, where $\mathbf{v}_{\perp j}$ represents only the drift motion. A contribution of the constant magnetic field energy B_0^2 is excluded in Eq. (53).

4. THE ELECTROMAGNETIC ION BEAM–PLASMA INSTABILITY

The first application of the closely-coupled implicit method to the low-frequency nonlinear plasma phenomena is a one-dimensional simulation of the electromagnetic ion beam–plasma instability. When a tenuous ion beam propagates along the ambient magnetic field through a dense background plasma in a velocity faster than the Alfven speed v_A, the electromagnetic ion–ion beam–plasma instability is excited [26]. The instability was investigated in connection with the diffused solar wind ions reflected from the earth's bow shock. Also a hybrid-particle simulation with particle ions and massless electrons was performed to find the origin of these ions [27].

Formerly, the hybrid simulation with particle ions and massless electrons used to be a major tool of simulating the low-frequency electromagnetic waves and instabilities. Implicit assumptions behind the hybrid simulations are (1) the quasi charge-neutrality of the plasma, (2) no electron orbit effects, and (3) instantaneous relaxation (adjustment) of the electrons. Since the electron inertia and orbit motions are ignored, particle and energy transport of the electrons along the magnetic field is beyond the scope of the hybrid simulation. This situation occurs, for example, in the parallel shocks, where the electrons are allowed to move freely along the magnetic field. By contrast, in the closely-coupled implicit method, the electrons are treated as independent particle species so that their relaxation along the magnetic field is naturally taken into account.

The dispersion equation for the electromagnetic ion beam–plasma instability propagating along the ambient magnetic field is given by [26, 27]

$$\omega^2 - c^2k^2 + \sum_j \omega_{pj}^2 \frac{\omega - kV_{dj}}{kv_j} Z\left(\frac{\omega - kV_{dj} + \omega_{cj}}{kv_j}\right) = 0, \qquad (54)$$

where $\omega_{pj} = (4\pi n_j e_j^2/m_j)^{1/2}$, $\omega_{cj} = e_j B/m_j c$ are the plasma and cyclotron frequencies of the jth species, respectively. $Z(\xi)$ is the plasma dispersion function, $v_j = (2T_j/m_j)^{1/2}$ is the thermal speed, and V_{dj} is the drift velocity along the ambient magnetic field. There are two unstable roots to Eq. (54) which are either resonant ($kV_d > 0$) or nonresonant ($kV_d < 0$). The resonant mode has a larger growth rate and its typical frequency, growth rate, and wavenumber in the $V_d/v_A \gg 1$ and $n_b/n_0 \ll 1$ limits are $\omega_r/\omega_{ci} \sim 0.2$, $\omega_i/\omega_{ci} \sim (n_b/2n_0)^{1/3}$, and $kV_d/\omega_{ci} \sim 1$, respectively, where n_b is the density of the beam ions.

The parameters chosen in the HIDENEK simulation are the ion beam speed $V_d = 10v_A$, the beam density $n_b/n_0 = 0.015$, the ambient magnetic field strength $\omega_{ce}/\omega_{pe} = 10^{-3}$, and the electron plasma beta $\beta_e = 8\pi n_e T_e/B^2 = 1$ [28]. The electron and ion temperatures are the same, $T_i/T_e = 1$. The system is periodic

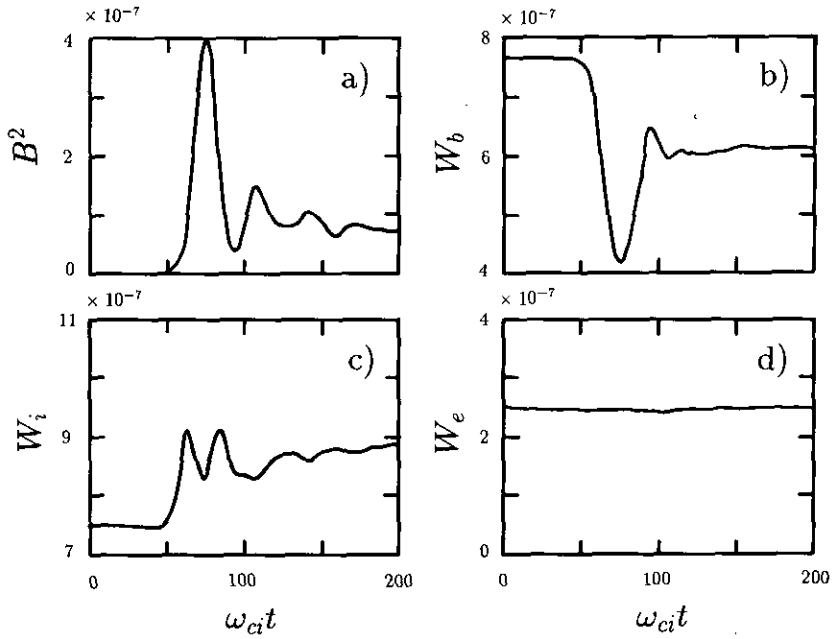

FIG. 1. The time histories of (a) the perturbed magnetic field energy; (b), (c) the kinetic energies of the beam and background ions, respectively; and (d) the parallel kinetic energy of the electrons for the electromagnetic ion beam–plasma instability with $v_d/v_A = 10$ and $n_b/n_0 = 1.5 \times 10^{-2}$.

along the ambient magnetic field (z-direction) with the length $L_z = 2560c/\omega_{pe}$ and 128 space grids. The mass ratio is $m_i/m_e = 100$ and the number of particles for each species is 16,384. The time step is $\omega_{pe}\Delta t = 2500$. The decentering parameter is $\alpha = 0.6$. A numerical filter is not applied. These parameters correspond to $\omega_{ci}\Delta t = 2.5 \times 10^{-2}$, $v_e \Delta t/\Delta z \cong 0.13$, and $\Delta z/\lambda_e \cong 3 \times 10^4$ with $\lambda_e = v_e/\sqrt{2}\,\omega_{pe}$ being the Debye length.

Figure 1 shows the time histories of the perturbed magnetic field energy, the kinetic energies of the beam and background ions, and the parallel kinetic energy of the electrons. The instability grows exponentially and the magnetic field energy peaks around $\omega_{ci}t \sim 70$. The electric field energy is roughly $(v_A/c)^2$ times that of the magnetic field energy. Later the magnetic energy decays to a quarter level compared to the primary peak and small peaks follow the primary one periodically. Large decrease in the beam kinetic energy occurs in coincidence with the growth of the instability. The background ions are heated roughly by 20%, but the electrons are hardly affected. As is found by comparing Figs. 1a–c, the beam kinetic energy is mainly converted to the magnetic energy and to some extent to the background ions at the growth of the instability and vice versa during the relaxation oscillations.

The large decrease in the kinetic energy of the beam ions is attributed to the decrease in the drift speed (Fig. 2a). Except for a temporary recovery of the beam speed at $\omega_{ci}t \sim 90$, the beam speed continues to decrease. This reveals that a part of the drift energy irreversibly goes to the thermal energy of both the beam and background ions. Conservation of the total energy slightly degrades at the growth of the instability which is expected from the discussions in Section 3.3. However, the total energy deviates by 5% during the saturation of the instability and it recovers to within 2% in the later times.

The electromagnetic field at the saturation time of the instability $\omega_{ci}t = 80$ is shown in Fig. 3. The observed wave that is excited by the instability is circularly polarized and is consistent with the linearly most unstable mode ($m = 4$–5) of the electromagnetic ion beam–plasma instability. The electric field looks somewhat jagged because the numerical filter has not been applied. But, the phase relation between the corresponding pairs of the electromagnetic field looks fine, i.e., $B_x \sim -E_y$, $B_y \sim E_x$. The frequency and the growth rate are measured to be $\omega/\omega_{ci} \cong 0.22 + 0.15i$ for the mode $m = 5$ which are in reasonable agreement with the theoretical value $\omega^{th}/\omega_{ci} = 0.23 + 0.19i$.

The nonlinear behavior of the beam ions is shown in the particle scatter plots of Fig. 4. The ions sitting initially around $V_d = 10v_A$ (Fig. 4a) are significantly affected by the instability as shown in Fig. 4b for $\omega_{ci}t = 80$. Obviously, the average beam speed has drastically decreased. When viewed in the $(v_z, v_\perp)$ space, the beam ions are scattered in the pitch-angle and they finally become equally distributed along the arc whose center is located on the $v_\perp = 0$ axis at $(v_A, 0)$. Formation of the equally distributed arc is clearly

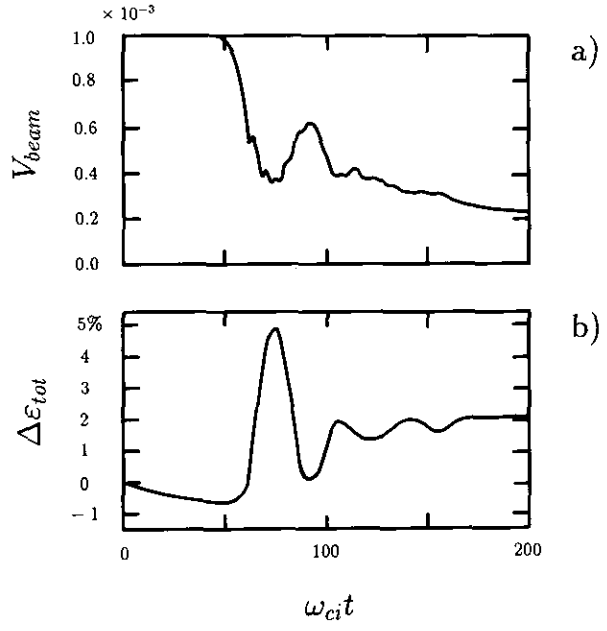

FIG. 2. The time histories of (a) the average drift speed of the beam ions and (b) the deviation of the system total energy in percent for the run shown in Fig. 1.

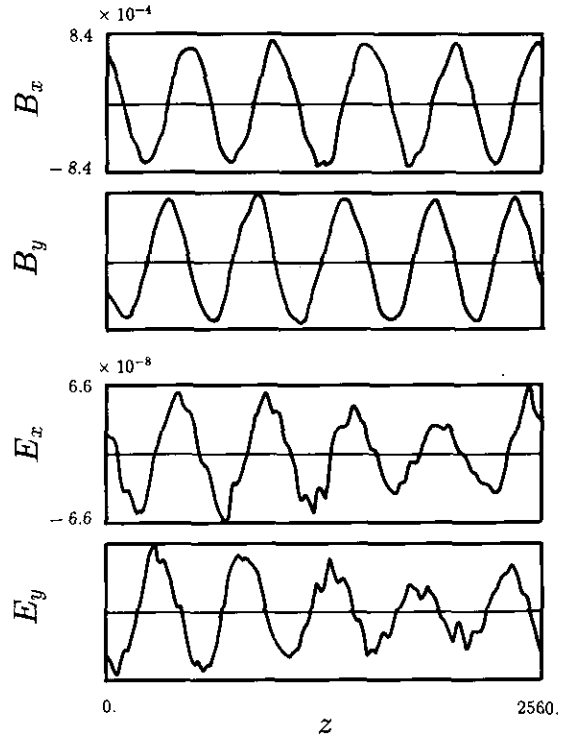

FIG. 3. The electromagnetic field B_x, B_y, E_x, and E_y from top to bottom, respectively, at $\omega_{ci}t = 80$ of the electromagnetic ion beam–plasma instability.

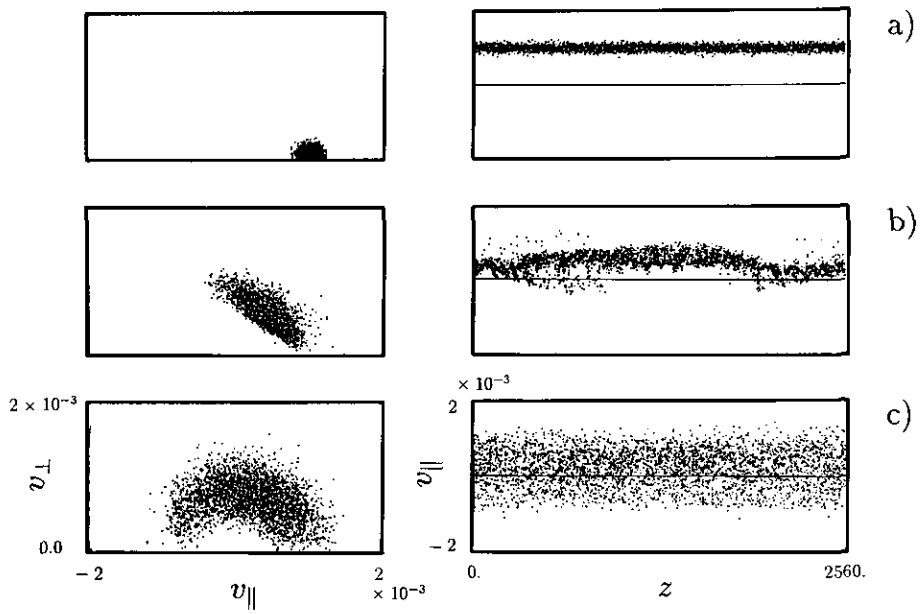

FIG. 4. The distribution of the beam ions in the $(v_z, v_\perp)$ and (z, v_z) spaces in the left and right columns, respectively, for (a) $\omega_{ci}t = 0$, (b) $\omega_{ci}t = 80$, and (c) $\omega_{ci}t = 200$.

seen at $\omega_{ci}t = 200$ in Fig. 4c. As noted previously, the electrons behave almost adiabatically. Although the electrons carry substantial $E \times B$ current in the perpendicular direction, they are hardly affected and heated by the instability because the wave frequency is by orders of magnitude smaller than the electron cyclotron frequency, $\omega/\omega_{ce} \ll 1$.

Before closing this section, a comparison of the present results with those of other implicit and hybrid particle codes is briefly made. The difference between the HIDENEK and CELEST codes is that the former chooses the magnetic field $\mathbf{B}^{n+\alpha}$ in the equations of motion and optionally the guiding-center approximation to the electrons, whereas the fully kinetic electrons and $\mathbf{B}^n$ are used in the latter [13]. The hybrid simulation requires artificial viscosity to control (damp out) spiky oscillations in the perturbed magnetic field, especially when the ambient magnetic field lies close to the simulation plane [27], which makes the simulation results somewhat artificial. Despite these differences, the growth and saturation of the instability and associated nonlinear results such as scattering of the beam ions and decrease in the beam drift speed have agreed generally well among the three simulations of the electromagnetic ion beam–plasma instability. The detailed comparison will be made elsewhere.

5. THE ANISOTROPY-DRIVEN ALFVEN-ION-CYCLOTRON INSTABILITY

As the second application of the HIDENEK code, the simulation of the Alfven-ion-cyclotron (AIC) instability is shown. A source of the free energy for this instability is the ion temperature anisotropy. The AIC instability is generated at the neutral beam injection into tokamaks [29, 30] and in association with very anisotropic ions in the foreshock region and the dayside region of the magnetosphere of the earth [31–33]. The AIC instability was shown to play a major role in generating the backstreaming ("reflected") ions from the earth's bow shock [31].

The dispersion equation of the Alfven-ion-cyclotron wave which propagates parallel to the ambient magnetic field is given by

$$\omega^2 - c^2k^2 + \omega_{pe}^2\left(\frac{\omega}{kv_e}\right)Z(\xi_e) + \omega_{pi}^2\left(\frac{\omega}{kv_{i\|}}\right)Z(\xi_i) - \omega_{pi}^2\left(1 - \frac{T_{i\perp}}{T_{i\|}}\right)[1 + \xi_i Z(\xi_i)] = 0, \tag{55}$$

where $\xi_e = (\omega \pm |\omega_{ce}|)/kv_e$, $\xi_i = (\omega \mp \omega_{ci})/kv_{i\|}$, and v_e, v_i are the thermal speeds of the electrons and ions, respectively. The perpendicular temperature of the ions, $T_{i\perp}$, is defined by

$$T_{i\perp} = 2\pi \int_{-\infty}^{\infty} dv_\| \int_0^{\infty} dv_\perp v_\perp \left(\tfrac{1}{2}m_i v_\perp^2\right) f_i(v_\|, v_\perp). \tag{56}$$

Here $f_i(v_\|, v_\perp)$ is the velocity distribution function of the ions. When the perpendicular temperature is larger than the parallel temperature, i.e., $(T_\perp/T_\|)_i > 1$, the AIC waves become unstable. The typical frequency in the

large anisotropy limit is $\omega_r/\omega_{ci} \sim 1$, the growth rate is $\omega_i/\omega_{ci} \sim (\beta_{i\perp}/2)^{1/2}$, and the wavenumber is $ck/\omega_{pi} \sim 1$, where $\beta_{i\perp} = 8\pi n_i T_{i\perp}/B^2$ is the ion beta value in the perpendicular direction. The aforementioned dispersion equation implies that any ion velocity distribution with the same temperature anisotropy is equivalent in generating the AIC instability [29, 31].

At the beginning of each simulation, the ions are loaded so that their temperature anisotropy becomes $(T_\perp/T_{||})_{i0} = 5$–$20$. The electrons are loaded isotropically. The other parameters are the system size $L_z = 120c/\omega_{pe}$, the electron thermal speed is $v_e/c = 0.2$, the temperature ratio is $T_{i||}/T_e = 1$, and the ambient magnetic field strength is $\omega_{ce}/\omega_{pe} = 0.7$. (Note that the electron cyclotron frequency does not appear in the simulation.) This corresponds to $\omega_{ci}/\omega_{pi} = 0.1$ for the choice of $m_i/m_e = 50$. The ion parallel beta value $B_{i||} = 8\pi n_i T_{i||}/B^2$ becomes approximately 8×10^{-2}. The system is periodic in the z-direction and the number of the space grids is 128. The number of particles for each species is 12,800, the time step is $\omega_{pe}\,\Delta t = 20$ ($\omega_{ci}\,\Delta t = 0.28$), and the decentering parameter is $\alpha = 0.6$. The quiet start technique of loading four particles in pairs is used to minimize the initial noise.

The time histories of the perturbed magnetic and electric field energies are shown in Fig. 5 for the $(T_\perp/T_{||})_i = 20$ case. The magnetic field grows exponentially out of the initial noise level and saturates around $\omega_{ci}t \sim 20$. For the electric field, since the electrostatic noise field initially dominates over the electromagnetic component, the instability appears to emerge abruptly at $\omega_{ci}t \sim 10$. The growth rate of the instability is measured to be $\omega_i/\omega_{ci} \sim 0.44$ for the most unstable mode ($m = 3$) with $ck/\omega_{pi} \sim 1.1$. This is in excellent agreement with the linear theory of the AIC instability, $\omega^{th}/\omega_{ci} = 0.84 + 0.45i$. Relaxation of the ion temperature anisotropy, $(T_\perp/T_{||})_i$, is shown in Fig. 5c. When the intensity of the perturbed magnetic field reaches a certain level, i.e., $\langle \delta B^2 \rangle / 8\pi n T_i \cong 1 \times 10^{-2}$, the temperature anisotropy begins to decrease. This process occurs in a relatively short time scale, $13\omega_{ci}^{-1}$ for the $(T_\perp/T_{||})_{i0} = 20$ case.

The total energy of the system decreases by a few percent as shown in Fig. 5d. The decrease in the total energy is clearly associated with the buildup of the electric field energy due to the growth of the instability. After the instability saturates around $\omega_{ci}t \sim 20$, the decrease in the total energy becomes slower. This behavior of the total energy is consistent with the argument in Section 3.3; the first integral of Eq. (52) vanishes in the periodic system, and the second integral which is positive definite becomes largest when the electromagnetic field amplitude changes rapidly. Hence, $|dW_{tot}/dt|$ takes the maximum value at this stage.

A series of ion scatter plots in the $(v_{||}, v_\perp)$, $(z, v_{||})$, and (z, ψ) spaces in Fig. 6 shows a remarkable pitch angle scattering of the anisotropic ions during $\omega_{ci}t = 10$–20. Here,

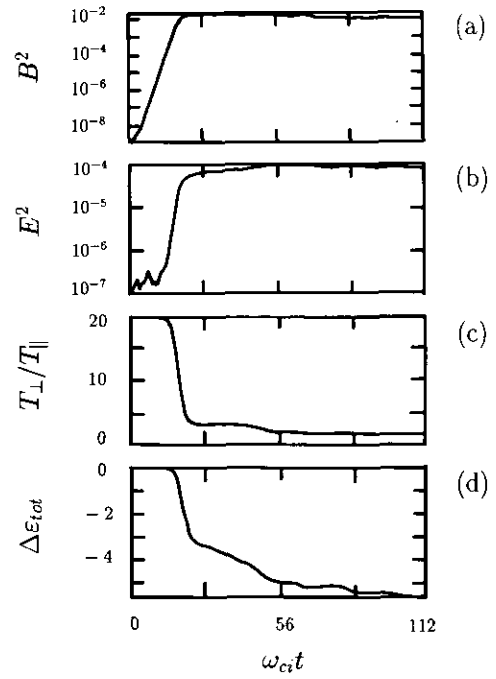

FIG. 5. The time histories of (a) the perturbed magnetic field energy, (b) the electric field energy, (c) the temperature anisotropy $(T_\perp/T_{||})_i$, and (d) the deviation of the total energy (in percent) for the Alfven-ion-cyclotron instability of the initial anisotropy $(T_\perp/T_{||})_{i0} = 20$.

$\psi = \tan^{-1}(v_y/v_x)$ is the phase angle of the perpendicular velocity of the ions. This scattering is most clearly observed at the change in the ion distribution in the $(v_{||}, v_\perp)$ space; the distribution evolves from the initial needle-like distribution into an isotropized, round-shaped distribution. The anisotropy becomes completely relaxed by $\omega_{ci}t \sim 50$. This pitch-angle scattering is the origin of the decrease in the temperature anisotropy shown in Fig. 5c.

In order to check the relaxed final temperature anisotropies, several runs are made systematically. The run with the small anisotropy $(T_\perp/T_{||})_{i0} = 5$ requires a long run up to $\omega_{ci}t \sim 300$ to have a complete relaxation of the anisotropy. For the $(T_\perp/T_{||})_{i0} = 20$ case, another run is performed with a longer system size $L_z = 240c/\omega_{pe}$ because the longer wavelength modes can be still unstable in the late stage of the instability with reduced anisotropy. The anisotropy ceases to decrease completely at $\omega_{ci}t \sim 70$. The final temperature anisotropies thus obtained for the initial anisotropies of 5, 10, and 20 are, respectively, 2.0, 1.8, and 1.9. The fact that the relaxed temperature anisotropy, $(T_\perp/T_{||})_i \cong 2$, is almost independent of the initial temperature anisotropies agrees with previous literature [29, 31].

A more interesting observation is the modulation of the ions and electrons both in the velocity and configuration spaces. The ion modulation in the phase space (z, ψ) at the end of the linear stage (Fig. 6b) is in-phase with the

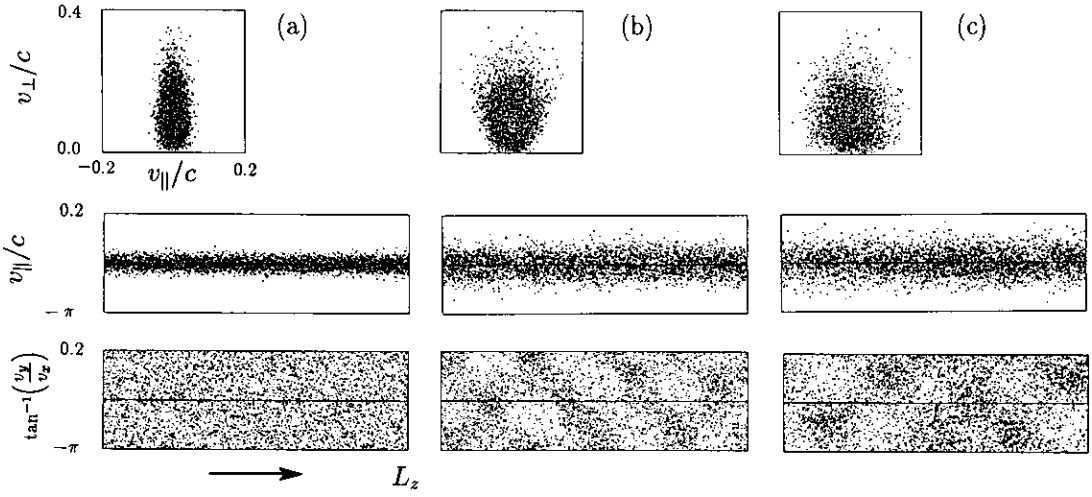

FIG. 6. The distribution of the ions in the $(v_\parallel, v_\perp)$, $(z, v_\parallel)$, and (z, ψ) spaces from top to bottom, respectively, for (a) $\omega_{ci}t = 0$, (b) $\omega_{ci}t = 21$, and (c) $\omega_{ci}t = 42$ ($\psi = \tan^{-1}(v_y/v_x)$).

magnetic perturbation and by 90 degrees out-of-phase with the electric field of the AIC wave. Afterwards in the nonlinear stage, the density modulation develops. A good spatial correlation is found between the ion density modulation and the intensity of the magnetic field $|\delta \mathbf{B}|^2 (z)$; the ion

$(x,\ y,\ z,\ v_x,\ v_y,\ v_z)$. The size of the simulation box is $L_x = L_y = 100c/\omega_{pe}$ and $L_z = 2000c/\omega_{pe}$ with $27 \times 27 \times 32$ grids. The x- and y-directions are limited by conducting walls and both the ends of the z-direction are periodically connected to each other. The average number of super-par-

pressure. The drift speed and the plasma temperatures must be consistently chosen so that the pressure balance $n(T_e+T_i)+B^2/8\pi=$ const. be satisfied radially. Otherwise, a rapid pinch (or expansion) of the initially-loaded plasma results in the finite-beta plasma simulation.

Other parameters are the ambient magnetic field strength $\omega_{ce}^{(0)}/\omega_{pe}=1$, the temperature ratio $T_e/T_i=1$, and the electron beta value $\beta_e=8\pi\bar{n}_eT_e/B^2=0.04$. The mass ratio is $m_i/m_e=400$ and the time step is $\omega_{pe}\Delta t=100$ (i.e., $\omega_{ci}\Delta t\sim 0.25$). The implicitness parameter is $\alpha=0.6$. The safety factor of the plasma, which is the ratio of the number of toroidal rotation of the magnetic field line to that of its poloidal rotation, becomes $q^{(0)}(r)\approx 0.6$ at the radial distance $r=L_n$. Thus, a helical rotation is initially present in the magnetic field structure (not in the current). By contrast to one-dimensional simulations in Sections 4 and 5, a digital filter is introduced to smooth the source terms of the CCFP equations. The digital filter helps to reduce the fluctuating electric field level arising from a grid-to-grid scale charge separation of plasma particles for which the finite spatial-differencing does not have a correct resolution. The weight of sampling for the consecutive five points along one direction is $(-\frac{1}{16}, \frac{4}{16}, \frac{10}{16}, \frac{4}{16}, -\frac{1}{16})$ (cf. Appendix of [5]) and the digital filter is applied once to each direction in a trilinear fashion.

The simulation run has been continued up to $\omega_{pe}t=2.6\times 10^4$ or $t=3.5\tau_A$. Here, the poloidal Alfven time is defined by $\tau_A=2L_n/v_{Ap}\sim 7.4\times 10^3\omega_{pe}^{-1}$ with $v_{Ap}=B_p/(4\pi m_i n)^{1/2}$ being the poloidal Alfven speed. The time history of the magnetic field energy is shown in Fig. 8a (the constant part $(B_0)^2$ has been omitted). A sudden increase in the magnetic field energy takes place at the beginning of the simulation. This is a self-adjustment of the beam–plasma system because the initial current flows in the z-direction which is not exactly along the helical magnetic field. The magnetic field energy increases gradually to $t=3.5\tau_A$. The

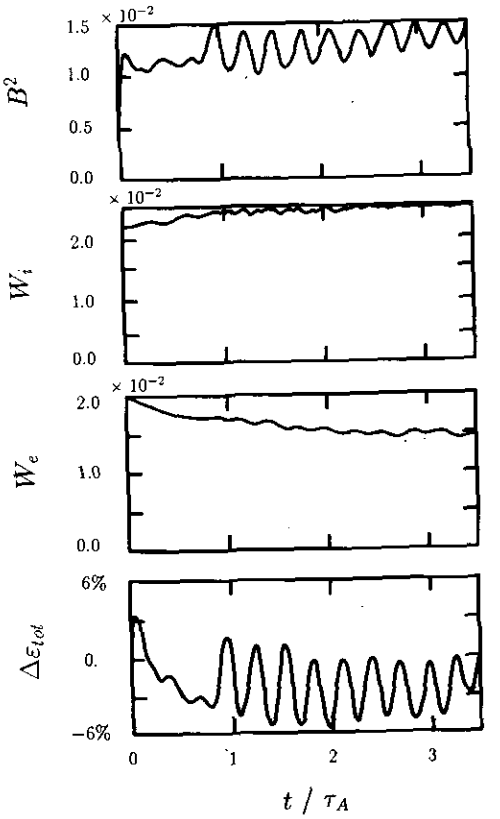

FIG. 8. The time histories of (a) the magnetic field energy, (b) the ion kinetic energy, (c) the electron kinetic energy defined by $W_e=\frac{1}{2}m_e\bar{v}_{\parallel}^2+\mu\bar{B}$, and (d) the deviation of the system total energy (the constant part $(B_0)^2$ is excluded in ε_{tot}).

electric field energy is dominated by the component due to the radial electric field which appears to be almost independent of the instability. The ion kinetic energy in Fig. 8b increases slightly during the simulation which is attributed to an increase in the perpendicular temperature. On the other hand, the electron kinetic energy decreases monotonically

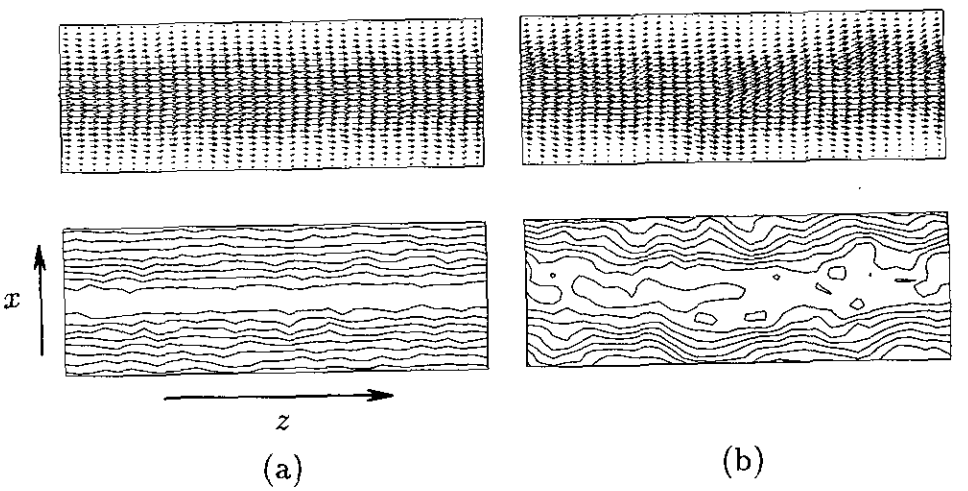

FIG. 9. The cross sections (at $y=\frac{1}{2}L_y$) of the current and charge densities in the upper and lower panels, respectively, at (a) $t=0.27\tau_A$ and (b) $t=3.2\tau_A$.

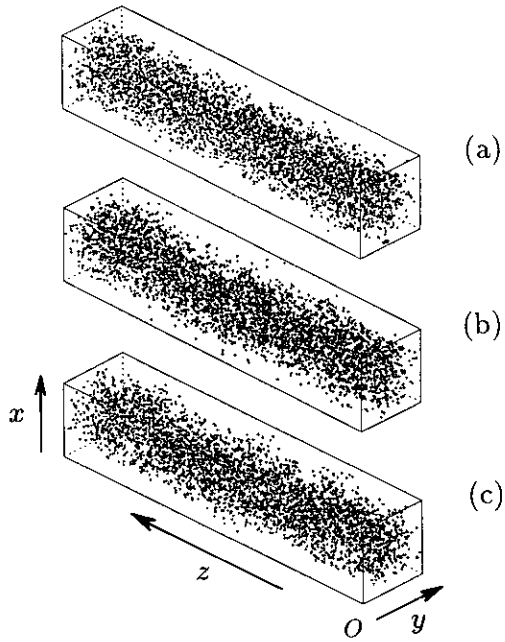

FIG. 10. The bird's-eye-view scatter plots in the (x, y, z) space at (a) $t = 0.27\tau_A$ and (b), (c) $t = 3.2\tau_A$. The plots are for the ions except for the electrons in (c). The helical perturbation has the mode number $m/n = 1/1$. (Note the length in the z-direction has been squeezed).

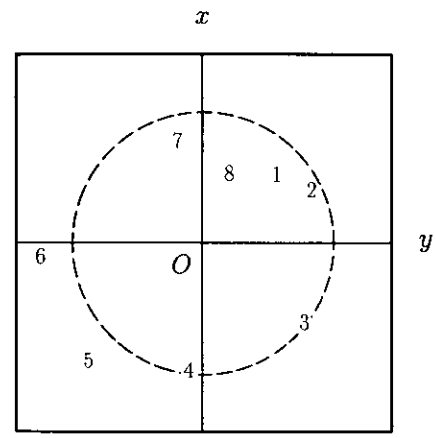

FIG. 11. A hodogram plot of the center of the beam axis at $t = 3.2\tau_A$. The number i corresponds to the toroidal position $z = iL_z/8$.

which arises from a decrease in the parallel temperature. This is considered to be an artificial cooling caused by incomplete Debye shielding. The total energy of the system deviates about $\pm 5\%$ during the simulation as shown in Fig. 8d.

The cross-sectional plots of the current and charge densities of the ions at the mid-plane ($y = L_y/2$) are shown in Fig. 9 for (a) $t = 0.27\tau_A$ and (b) $t = 3.2\tau_A$. The left-hand side panels correspond to the early state after the initial transient motions have subsided. In the right-hand side panels, we can see a deformation of the beam current which has been projected to the toroidal mid-plane. The dominant mode number of the deformation in the z-direction is found to be $n = 1$. The whole aspect of the deformation of the beam current is better observed in the bird's-eye-view scatter plots of ions and electrons in Fig. 10. The top panel is the plot for the ions at $t = 0.27\tau_A$ and the middle and bottom panels show the ion and electron species at $t = 3.2\tau_A$, respectively. Almost the same spatial distortions are observed both in the electrons and ions. Here, it is found that the aforementioned deformation is a helical perturbation which is occurring in the three-dimensional space.

Figure 11 is a hodogram plot of the location of the beam center. The toroidal direction is divided to eight bins and the positions of the ions (x_j, y_j) in each bin are averaged. The number i in the figure is the bin number which corresponds to the z-position $z = iL_z/8$. The center of the circle in the figure coincides with that of the poloidal cross section and its radius is $3.5c/\omega_{pe}$. It is seen that, except for a strayed and slow movement around 8-1-2, the beam axis rotates in the clockwise direction toward the positive z-direction. This helical pitch is the same as that of the initial magnetic field. The mode number of the helical distortion of the beam axis is determined to be $m/n = 1/1$.

The poloidal component of the magnetic field is shown in the consecutive poloidal cross-sectional plots at $t = 3.2\tau_A$ (Fig. 12). The toroidal separation between the two adjacent cross-sections is $\frac{1}{4}L_z$. The center of the magnetic axis

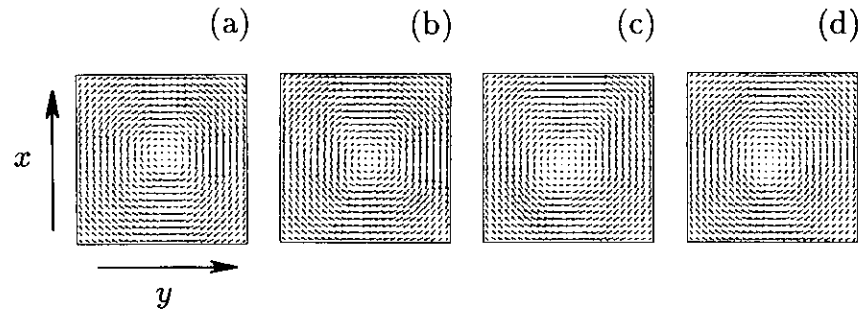

FIG. 12. The poloidal magnetic field (B_x, B_y) in the consecutive poloidal cross sections (toroidal separation of $L_z/4$) at $t = 3.2\tau_A$. The maximum amplitude of the poloidal magnetic field is 0.21 in the simulation unit.

(null point of the poloidal magnetic field) is seen to shift in the poloidal cross sections. Plotting the locations of the magnetic axis, as we did for the beam axis, again shows a clockwise rotation of the magnetic axis toward the z-direction. By considering the plasma geometry used in the simulation and the fact that the helical deformation of the beam and magnetic field has occurred in a few poloidal Alfven times, we can conclude that the present instability is the ideal (external) kink instability [36].

7. SUMMARY AND CONCLUDING REMARKS

7.1. Summary

A new and advanced plasma simulation method—the closely-coupled implicit method (HIDENEK), was described in this paper which is suitable for studies of low-frequency, large space-scale kinetic phenomena in the finite-beta, inhomogeneous plasmas. The present simulation method included the physical processes caused by the electron inertia and motions along the magnetic field which were totally ignored in the traditional hybrid particle simulations. The key of this implicit method consisted in the completely implicit, CCFP equations which were free from the Courant condition. These equations were derived by combining the equations of motion and the Maxwell equations. In order to incorporate the diamagnetic and magnetization effects while eliminating both the plasma and cyclotron frequencies of the electrons, the slightly backward time-decentered scheme and the guiding-center approximation to the electrons were adopted. The code was successfully implemented in the HIDENEK code from one to three dimensions.

In the present simulation method, the electromagnetic field was solved in the real (configuration) space for better treatment of the coupled field-particle equations. A very efficient and accuracy-preserving approximation was introduced in Section 3 to the coupled summation terms over the particle and unknown field quantities. This made the solution of the CCFP equations possible under the limited computing resources while retaining the full kinetic flavor of the equations. For the solution of the huge matrix equation thus derived, the Gaussian elimination technique was applied in the one-dimensional simulations (Sections 4 and 5), and the bi-conjugate gradient method was used in the three-dimensional simulation (Section 6). The numerical stability and energy conservation of this implicit method against the implicitness parameter were also discussed in Section 3.

As a verification and demonstration of the application area of the closely-coupled implicit method, three physics applications were presented in Sections 4 and 5 for one dimension and in Section 6 for three dimensions. In the first two applications, the electromagnetic ion beam–plasma instability and the Alfven-ion-cyclotron instability were shown to be excited by tapping the free energy from either the drift motion of the ion beam or from the anisotropy of hot ions. In both cases, the ions suffered from a significant pitch-angle scattering and strong modulation in the velocity and configuration spaces. Precisely, in the first application, the drifting beam ions were substantially slowed down and scattered in the nonlinear stage of the instability. In the second application, the temperature anisotropy of the hot ions was completely isotropized by the self-excited circularly polarized electromagnetic waves; the anisotropy relaxed to $(T_\perp/T_\parallel)_i \approx 2$ irrespective of the initial temperature anisotropies. In the third application to the three-dimensional plasma, the density-peaked ion beam with the safety factor less than unity was shown to undergo a helical distortion by the external kink instability in the ideal magnetohydrodynamic time scale.

7.2. A Design of the Simulation Parameters

For the purpose of designing suitable simulation parameters, it would be useful to clarify the restrictions of the present simulation method with respect to the time step and the grid size. The first restriction on the time step arises from the necessity to accurately keep track of the ion cyclotron motion,

$$\omega_{ci}\,\Delta t \leqslant 0.2. \tag{57}$$

The second restriction is a transit time condition which is required to resolve the structure of the scale length $\lambda = 2\pi/k_{\parallel,\max}$,

$$k_{\parallel,\max} v_\parallel \,\Delta t \ll 1, \tag{58}$$

where $v_\parallel$ is the fastest speed along the magnetic field. The third restriction appears in the combination of the time step and the grid size,

$$O(0.1) < v_\parallel \,\Delta t/\Delta x < O(1). \tag{59}$$

The lower inequality arises from an aliasing due to the coarse grid instability [5, 11] and the upper inequality from the accuracy of the expansion used in Eq. (30) and that of the predicted particle position $\bar{\mathbf{x}}_j^{n+1/2}$ (see just below Eq. (12)). Actually, the second restriction (58) can be similar to the upper inequality of Eq. (59).

A slight difference of the predicted particle position $\bar{\mathbf{x}}_j^{n+1/2}$ which is used to evaluate the particle position $\mathbf{x}_j^{n+1/2}$ can also be a source of numerical heating of the plasma. The difference of the two positions for the electrons, which

can be more relevant than the ions because of their large thermal velocity, is written as

$$\delta \mathbf{x}_D \equiv \mathbf{x}_j^{n+1/2} - \bar{\mathbf{x}}_j^{n+1/2} \tag{60}$$

$$\cong \left(\frac{1}{2}\Delta t\right)^2 \frac{(-e)}{m_e}(\mathbf{E}_{\parallel}^{n+\alpha} - \mathbf{E}_{\parallel}^{n}) + \frac{1}{2}\Delta t\,(\mathbf{v}_{\perp}^{n+\alpha} - \mathbf{v}_{\perp}^{n}). \tag{61}$$

The restriction may be given in the form of the accuracy condition

$$\frac{|\delta \mathbf{x}_D|}{\Delta x} \cong \frac{\Delta t}{2\Delta x}\left|\left\{\frac{1}{2}\Delta t \frac{(-e)}{m_e}(\mathbf{E}_{\parallel}^{n+\alpha} - \mathbf{E}_{\parallel}^{n}) + (\mathbf{v}_{\perp}^{n+\alpha} - \mathbf{v}_{\perp}^{n})\right\}\right| \ll 1. \tag{62}$$

The electric field in Eq. (62) includes both the physically evolving component and the thermal fluctuation due to particle discreteness. If we assume a monochromatic sinusoidal wave, $E_{\parallel}^{n} \sim e^{i\omega n \Delta t}$ for the physical component, we have

$$E_{\parallel}^{n+\alpha} - E_{\parallel}^{n} \approx i\alpha\omega\,\Delta t\, E_{\parallel}^{n}. \tag{63}$$

Since $\omega\,\Delta t \ll 1$ holds for the physically resolved modes in the simulation, $|\delta \mathbf{x}_D|$ can be negligibly small compared with the cell size if the value $(v_{th}\,\Delta t/\Delta x)$ is chosen to be of the order of unity $(eE_{\parallel}\,\Delta t/m_e \leqslant v_{th})$. However, with too few particles per cell, the deviation due to the fluctuating electric field may be as large as

$$\frac{|\delta \mathbf{x}_{D,n}|}{\Delta x} \approx \frac{\Delta t}{2\Delta x}\left|\left\{\frac{1}{2}\Delta t \frac{(-e)}{m_e}\mathbf{E}_f + \mathbf{v}_{\perp,f}\right\}\right|. \tag{64}$$

This deviation can be small compared to unity if the acceleration due to the fluctuating electric field is kept small such that

$$\Delta t\,|(e/m_e)\,\mathbf{E}_f| \ll v_{th}. \tag{65}$$

Summarizing the above arguments, the following procedure may be constructed for the choice of the simulation parameters. First, we note that there are often characteristic spatial scale-lengths in the plasma phenomena, especially in the wave and instability problems. The grid size is then determined from a resolution requirement. Next, if we specify the magnetic field strength and the electron beta value, the electron thermal speed is determined by

$$\frac{v_e}{c} = \sqrt{\beta}\,\frac{\omega_{ce}}{\omega_{pe}}. \tag{66}$$

Referring to the conditions Eqs. (58) and (59), the range of an allowable time step is determined against the chosen space-grid size. Here, of course, the physics condition $\omega_0\,\Delta t \ll 1$ must be satisfied, where ω_0 is the characteristic frequency of the phenomena. It is also appropriate to follow condition Eq. (65) in order to minimize artificial heating of the plasma, with which the upper limit of the time step or the minimum number of simulation particles are estimated Although there are several restrictions on the time step to be accounted for, it is not so difficult to find an appropriate time step. Finally, the condition Eq. (57) is referred to in order to determine the lower limit of the mass ratio (m_i/m_e). At this stage, all the parameters may have to be reshuffled to expand their allowable range of variation or to fit the simulation run into the given computing resources.

7.3. Technical Remarks

Several remarks and future plans are mentioned here concerning the closely-coupled implicit method (HIDENEK). First, it is important to use the identical formula in the equations of motion and the corresponding parts in the CCFP equations. This must be kept in mind when one wishes to modify or extend the present algorithm. Second, the same area-weighting scheme should be applied both in the evaluation of the electromagnetic field at the particle position and in the assignment of the particle information to the space grids. A violation to these rules causes poor momentum and energy conservation and makes the simulation susceptible to numerical instabilities.

It was stated in Section 2 that the magnetic field $\mathbf{B}^{n+\alpha}$ of the time level $t = t^{n+\alpha}$ is used instead of $\mathbf{B}^n$ in the equations of motion. The consistency of this choice may be verified in the following example. Let us consider a monochromatic Alfven wave in one dimension, i.e., $\mathbf{E}_k$, $\mathbf{B}_k \propto \exp[i(kz - \omega t)]$. Both the perturbed electric and magnetic fields are perpendicular to the wave vector that points to the z-direction. A numerator of the $\mathbf{E} \times \mathbf{B}$ drift term is written

$$\mathbf{E}_k \times \mathbf{B}' = \mathbf{E}_k \times \mathbf{B}_0 + \mathbf{E}_k \times ((c/\omega)\mathbf{k} \times \mathbf{E}_k'), \tag{67}$$

where $(')$ stands for a time level $t = t'$ and non-$(')$ quantities are defined at $t = t^{n+\alpha}$. Also Faraday's law $\mathbf{B}_k' = (c/\omega)\mathbf{k} \times \mathbf{E}_k'$ has been used. A difference due to the choice of the magnetic field's time level occurs in the second term of Eq. (67). For $t' = t^{n+\alpha}$, the second term becomes $\mathbf{v}_2 = (c\mathbf{k}/\omega)\,E_k^2$. However, for any choice of $t' \neq t^{n+\alpha}$, we have

$$\mathbf{v}_2' = (c\mathbf{k}/\omega)(\mathbf{E}_{\mathbf{k}} \cdot \mathbf{E}_{\mathbf{k}}') = (c\mathbf{k}/\omega)\,E_k^2 \cos(\omega\delta t)$$

$$\cong (c\mathbf{k}/\omega)\,E_k^2[1 - \tfrac{1}{2}(\omega\delta t)^2], \tag{68}$$

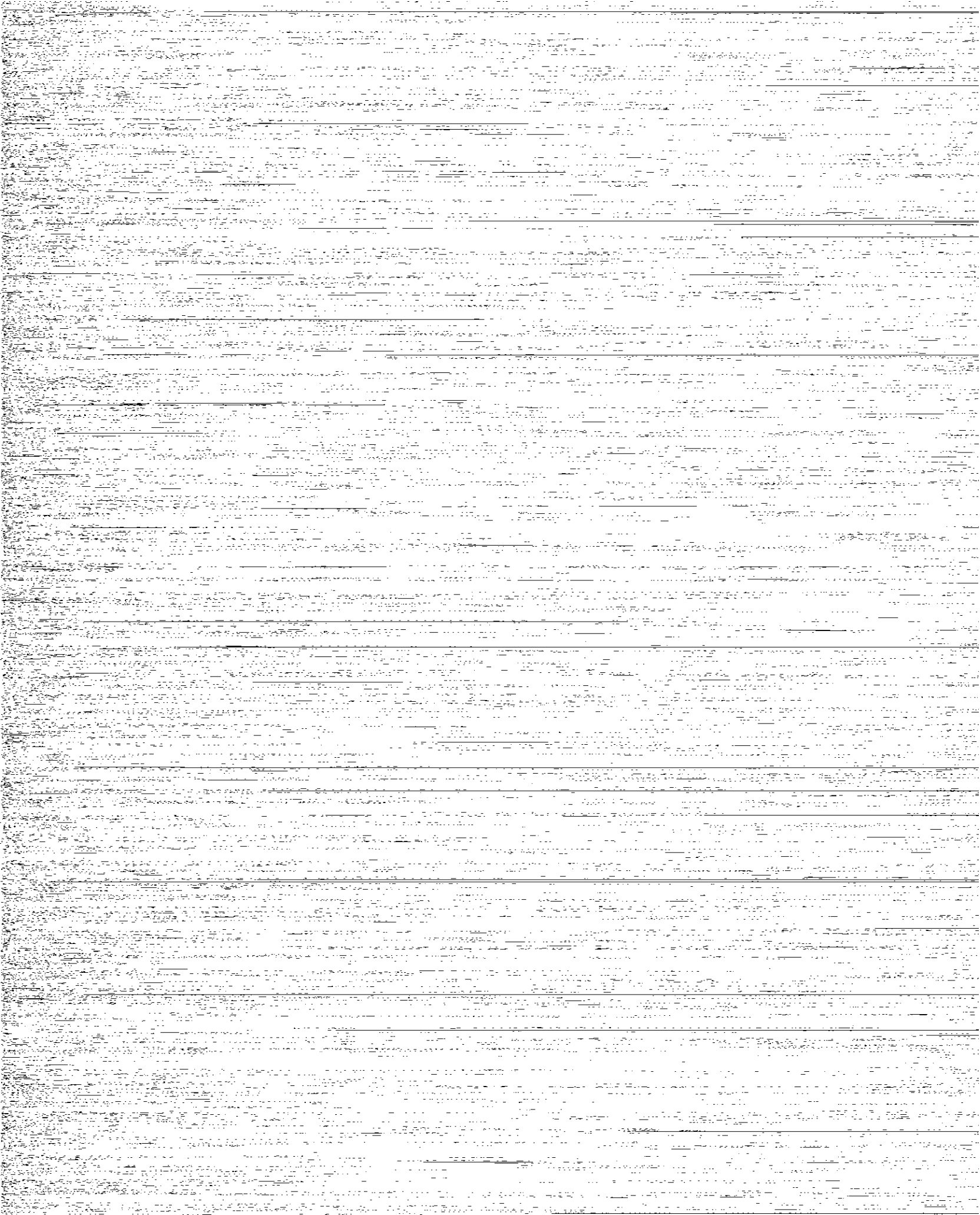

6. J. U. Brackbill and B. I. Cohen (Eds.), *Multiple Time Scales* (Academic Press, New York, 1985), Chaps. 7–11.
7. M. Tanaka, *J. Comput. Phys.* **79**, 209 (1988).
8. W. W. Lee, *J. Comput. Phys.* **72**, 243 (1987).
9. R. J. Mason, *J. Comput. Phys.* **47**, 233 (1981).
10. J. Denavit, *J. Comput. Phys.* **42**, 337 (1981).
11. J. U. Brackbill and D. W. Forslund, *J. Comput. Phys.* **46**, 271 (1982).
12. D. W. Forslund and J. U. Brackbill, *Phys. Rev. Lett.* **48**, 1614 (1982).
13. H. X. Vu and J. U. Brackbill, *Comput. Phys. Commun* **69**, 253 (1992).
14. M. Tanaka, *The 14th International Conference on Numerical Simulation of Plasmas, Annapolis, Sept. 1991.*
15. A. B. Langdon and D. C. Barnes, *Multiple Time Scales* (Academic Press, New York, 1985), Chap. 11.
16. D. W. Hewett and A. B. Langdon, *J. Comput. Phys.* **72**, 121 (1987).
17. A. Friedman, *J. Comput. Phys.* **90**, 292 (1990).
18. J. A. Byers, B. J. Cohen, W. C. Condit, and J. D. Hanson, *J. Comput. Phys.* **27**, 363 (1978).
19. M. M. Leroy, D. Winske, C. C. Goodrich, C. S. Wu, and K. Papadopoulos, *J. Geophys. Res.* **87**, 5081 (1982).
20. M. Tanaka, T. Sato, and A. Hasegawa, *Phys. Fluids B* **1**, 325 (1989).
21. M. Tanaka and T. Sato, *Phys. Fluids* **29**, 3823 (1986).
22. A. B. Langdon and B. F. Lasinski, *Methods Comput. Phys.* **16**, 327 (1976).
23. A. B. Langdon, *J. Comput. Phys.* **30**, 202 (1979).
24. J. U. Brackbill and H. X. Vu, private communication, 1992.
25. M. R. Hestenes and E. Steifel, *J. Res. NBS* **49**, 409 (1952); H. Toda, *The Bi-conjugate Gradient Method* (Kyoiku, Tokyo, 1990).
26. P. Gary, C. W. Smith, M. A. Lee, M. L. Goldstein, and D. W. Forslund, *Phys. Fluids* **27**, 1852 (1984).
27. D. Winske and M. M. Leroy, *J. Geophys. Res.* **89**, 2673 (1984).
28. The simulation here uses the same parameters as that in Ref. [13].
29. R. C. Davidson and J. M. Ogden, *Phys. Fluids* **18**, 1045 (1975).
30. T. Tajima, K. Mima, and J. M. Dawson, *Phys. Rev. Lett.* **39**, 201 (1977).
31. M. Tanaka, C. C. Goodrich, D. Winske, and K. Papadopoulos, *J. Geophys. Res.* **88**, 3046 (1983).
32. M. Tanaka, *J. Geophys. Res.* **90**, 6459 (1985).
33. Y. Omura, H. Matsumoto, R. Gendrin, and M. Abdalla, *J. Geophys. Res.* **90**, 8281 (1985).
34. G. Statham and D. Ter Harr, *Plasma Phys.* **25**, 681 (1983).
35. H. Alfven, *Phys. Rev.* **55**, 425 (1939).
36. G. Bateman, *MHD Instabilities* (MIT Press, Cambridge, MA, 1978).